UCLA
UCLA Electronic Theses and Dissertations

Title

Deterministic control of magnetism by the multiferroic magnetoelastic effect at the nano- and micro-scale

Permalink

https://escholarship.org/uc/item/4zd038ng

Author

Sohn, Hyunmin

Publication Date

2017

Peer reviewed|Thesis/dissertation

UNIVERSITY OF CALIFORNIA

Los Angeles

Deterministic control of magnetism by the multiferroic magnetoelastic effect

at the nano- and micro-scale

A dissertation submitted in partial satisfaction of the

requirements for the degree Doctor of Philosophy

in Electrical Engineering

by

Hyunmin Sohn

2017

ABSTRACT OF THE DISSERTATION

Deterministic control of magnetism by multiferroic magnetoelastic effect

at the nano- and micro-scale

by

Hyunmin Sohn

Doctor of Philosophy in Electrical Engineering

University of California, Los Angeles, 2017

Professor Robert N. Candler, Chair

Ferromagnetic materials are being incorporated into a wider range of emerging applications of nanotechnology, which include memory, nanotweezers, microfluidics, and biomedical applications. These newer applications exploit the favorable scalability of the permanent magnetic diploes due to their relatively large energy density, in addition to their compatibility with fluidic environments. Previously, two major approaches have been studied to adapt magnetism at the nanoscale/microscale: scaling current-based magnetic coils, and employing external magnetic fields. However, Joule heating causes significant limitations in current-based magnetic devices, as devices are miniaturized below the microscale due to reduced efficiency and challenges of heat dissipation. Use of external magnetic field control requires external magnetic sources such as permanent magnets or electromagnetic coils, which do not

provide control at the individual element-level control and limit overall system scalability. Therefore, control of magnetism is one of the major challenges when scaling magnetic systems below the microscale

This work demonstrates a new approach to control of magnetization, or magnetic states in ferromagnetic structures using electrically generated strain. Strain coupling can be achieved by building ferromagnetic structures on piezoelectric substrates, which are called multiferroic heterostructures. Magnetic states at the nano- and micro-scale are investigated with finite element analysis (FEA) models. The magnetoelastic coupling of the magnetic states and electrically generated strain are numerically predicted by a FEA that fully couples Landau-Lifshitz-Gilbert micromagnetics with elastodynamics. This simulation results are validated by X-ray magnetic dichroism photoemission microscopy (XMCD-PEEM), and magnetic force microscopy (MFM). This work provides a new pathway to develop energy efficient magnetic manipulation techniques at the nanoscale.

The dissertation of Hyunmin Sohn is approved.

Gregory P. Carman

Oscar M. Stafsudd

Yuanxun E. Wang

Robert N. Candler, Committee Chair

University of California, Los Angeles

2017

For my beloved family and friends,

TABLE OF CONTENTS

LIST OF FIGURES

LIST OF TABLES

VITA

Education

2012   Master of Science in Electrical Engineering

                  University of California, Los Angeles

2003   Bachelor of Science in Electrical Engineering

                  Seoul National University, Seoul

Employment

2012-2017   Graduate Student Researcher

                  Sensors & Technology Lab

                  University of California, Los Angeles

2009-2010   Undergraduate Student Researcher

                  Integrated Systems Design Lab

                  Seoul National University, Seoul

PUBLICATIONS AND PRESENTATIONS

Journal publications

Hyunmin Sohn; M. E. Nowakowski; C. Liang; J. L. Hockel; K. Wetzlar; S. Keller; B. M. McLellan; M. A. Marcus; A. Doran; A. Young; M. Kläui; G. P. Carman; J. Bokor; R. N. Candler, *Electrically-driven magnetic domain wall rotation in multiferroic heterostructures to manipulate suspended on-chip magnetic particles*, in ***ACS Nano***, 2015, 9 (5), pp 4814–4826.

Yongha Hwang; **Hyunmin Sohn**; A. Phan; O. M. Yaghi; R. N. Candler, *Dielectrophoresis-Assembled Zeolitic Imidazolate Framework Nanoparticle-Coupled Resonators for Highly Sensitive and Selective Gas Detection*, ***Nano Lett.***, 2013, 13 (11), pp 5271–5276.

Hyunmin Sohn, *Strain-Mediated Electrical Control of Magnetization in Micron-scale Nickel Ring on PMN-PT*, **Hilton Head Workshop 2014**: A Solid-State Sensors, Actuators and Microsystems Workshop, Oral Presentation, Hilton Head Island, South Carolina, USA, 2014 June.

CHAPTER 1
INTRODUCTION

1.1 Control of magnetism at the small scale

With advances in the understanding of fundamental magnetism, technological applications of magnetism have become an integral part of modern life. It is not hard to find magnetic applications in our daily life, such as high-power electro-motors, generators, hard drives, medical magnetic resonance imaging (MRI), and magnetic levitation trains. With a growing demand for portable electronics in recent years, researchers seek for a way to adapt the prevalent electromagnetism at the micro- and nano- scale.

Recently, ferromagnetic materials are being considered for a wide range of emerging nano- and micro- applications, such as magnetic-based memory[1, 2], nanotweezers[3, 4], microfluidics[5, 6], and biomedical applications[7, 8], due to their ability to maintain spontaneous magnetization, provide relatively large energy density[9], and their compatibility with operation in fluids. Despite the growing need for magnetism at the small scale, control of magnetism at this level is still one of the challenging engineering problems. In this work, we demonstrate a scalable and energy-efficient way to control magnetism at the nanoscale/microscale.

1.1.1 Previous approaches

Previously, two major approaches have been studied to adapt magnetism at the nanoscale/microscale: scaling current-based magnetic coils[10], and employing external magnetic fields[6, 11]. However, Joule heating causes significant limitations in current-based magnetic devices, as devices are miniaturized below the microscale due to reduced efficiency and challenges of heat dissipation. Use of external magnetic field control requires external magnetic sources such as permanent magnets or electromagnetic coils, which do not provide control at the individual element-level control and limit overall system scalability. Therefore, the conventional control of magnetism has an apparent limit when scaling magnetic systems below the microscale.

1.2 Strain-mediated multiferroic heterostructures

Multiferroics is the study of materials, composites, or laminates that possess more than two ferroics properties, such as ferroelectricity, ferromagnetism, ferroeleasticity and ferrotoroidicity. Two major categories of multiferroics exist: single-phase multiferroics and multiferroic heterostructures. The history of multiferroics started with exploring single-phase materials that exhibit high ferroic properties. However, single-phase multiferroic materials intrinsically show the weak coupling between ferroic orders. Later, multiferroic heterostructures were created by integrating ferroelectric and magnetic materials through the exchange of elastic, electric, and magnetic energy[12]. Among many types of the multiferroic heterotructures, the development of strain-mediated multiferroic heterostructures has shown promising results that

are able to maximize electromagnetic coupling at the small scale[13-16]. Researchers combined ferroelectricity and ferromagnetism that are coupled via strain, called strain-mediated multiferroic coupling. The conceptual coupling diagram is shown in Figure 1.

Strain-mediated multiferroic heterostructures consist of piezoelectric and magnetoelastic materials that are coupled via strain transfer at their interfaces. Instead of using electric current or an external magnetic field to manipulate magnetization in the material, multiferroic composites use a piezoelectrically generated strain to control magnetization in nano/microstructures[17-25].

Because most of the previous studies adapted single crystal piezoelectric materials that generate a large piezoelectric strain along specific crystallographic directions[25, 26], the control of magnetism was confined by the crystallographic directions, with a lack of isotropic controllability. More recently, researchers suggested a way to generate isotropic strains with surface patterned electrodes on polycrystalline piezoelectric ceramics[27-30]. However, no experimental work to date has verified this type of control of magnetization in micro- and nanoscale structures.
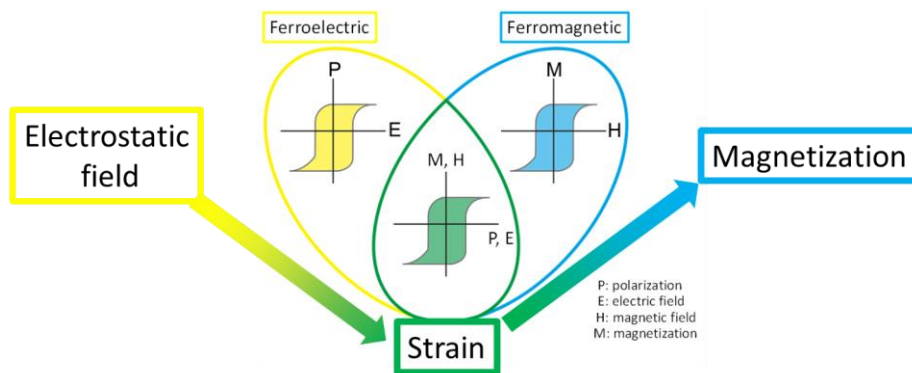
Figure 1 Diagram of strain-mediated multiferroic magnetoelectric coupling[13]

1.2.1 Magnetostrictive materials

Magnetostriction is a phenomenon found in ferromagnetic materials, such as Fe, Co, Ni, and their alloys. Ferromagnetic materials in a magnetic field rearrange their crystal structures so that an easy axis of magnetization is aligned with the field to minimize the free energy, which causes a mechanical displacement. This is quantified by the magnetostrictive constant, λ, defined as the fractional mechanical displacement ($\Delta l/l$). Depending on ferromagnetic materials, their magnitude and sign of magnetostriction constant are different. In Table 1, magnetostriction constants for selected ferromagnetic materials are shown. Tb-Dy-Fe alloy, Terfenol-D, exhibits the highest magnetostriction ($\lambda_S = 996$ ppm) but suffers from its brittle and highly reactive properties. Fe-Ga alloys, called Galfenol, have also been discovered to show a large magnetostriction up to 400 ppm. These rare earth alloys are promising candidates to maximize the magnetoelectric coupling in the multiferroic composites but still need more investigation on thin film deposition and microfabrication.

Reciprocally, applying a strain or stress on a magnetic material can change the magnetic energy landscape and change preferred magnetization directions. This effect is also called Villari effect. The Villari effect is the key to control magnetism in strain-mediated multiferroic composites. Applying a mechanical strain on a ferromagnetic material generates a magnetoelastic energy. The magnetoelastic energy in isotropic materials is given as

$$E_{m.e.} = -\frac{3}{2}\lambda_s E s \cos^2\theta \tag{1}$$

, where λ_s is saturation magnetostriction, E is Young's modulus, θ is the angle between the magnetization and strain, and s is the applied strain. The sign of λ_s determines whether magnetization favors compressive strain or tensile strain.

In single crystals, the magnetostriction is anisotropic, which depends on the direction of the crystal axes. Independent magnetostriction constants are defined along the principal axes, and the magnetostriction constant in other directions is calculated by a linear combination of the independent constants. For examples, in cubic materials, two independent λ_{100} and λ_{111} are measured along the <100> and <111> directions, respectively.

Table 1 Magnetostriction constants for different materials

Metal	Magnetostriction constants [ppm]		
	λ_{100}	λ_{111}	λ_s
Fe	21	-21	-7
Ni	-46	-24	-34
$Fe_{(1-x)}Ga_x$ (0.17≤x≤0.19) [31]	320	-	-
$Tb_{0.3}Dy_{0.7}Fe_2$	90	1600	996

1.2.2 Piezoelectric materials

Piezoelectric materials can create a mechanical deformation with the application of an electric field. They also work in reverse, changing electric polarization with a mechanical strain or stress. The piezoelectric effect was first discovered by Pierre and Paul-Jacques Curie in 1880.

The crystallographic symmetry of materials plays an important role in the piezoelectric effect. The piezoelectric effect is only observed in non-centrosymmetric crystals. However, not all non-centrosymmetric crystals show the piezoelectric effect. Of the 21 non-centrosymmetric crystal classes, 20 classes may exhibit the piezoelectricity. Among the piezoelectric crystal classes, 10 of them are pyroelectric, which possess spontaneous electric polarization, or net electric dipole moment, that varies with temperature. If spontaneous electric polarization in a pyroelectric material can be switched by an external electric field, this is classified in ferroelectric materials. Ferroelectric materials possess spontaneous polarization that strongly couples with crystal structures and mechanical deformation, and the polarization can be controlled by an external electric field.

Ferroelectric crystals and ceramics are widely used for many applications due to the linear electromechanical relationship. Ferroelectric ceramics consist of randomly oriented ferroelectric crystal grains. Due to their polycrystalline structure, the macroscopic piezoelectric constant is usually lower than that of ferroelectric crystals. However, compared to ferroelectric crystals, which require complicated growth processes, ferroelectric ceramics are much less expensive. In addition, because ceramics are macroscopically isotropic, ferroelectric ceramics can be used to generate isotropic strain with an external electric field.

Various ferroelectric crystals that show a giant piezoelectric effect have recently been discovered, such as PZN-PT and PMN-PT relaxor single crystals[26]. It was also shown that a giant piezoelectric response can be observed by poling a ferroelectric crystal along certain crystallographic directions[26].

The piezoelectric response can be calculated using the piezoelectric constitutive equations: strain-charge form as

$$S = s_E \cdot T + d^T \cdot E \tag{2}$$

$$D = d \cdot T + \varepsilon_E \cdot E \tag{3}$$

, where S is the strain, T is the stress, E is the electric field, and D is the electric displacement field, s_E is the material compliance, d is the piezoelectric coupling coefficient, and ε_E is the electric permittivity.

1.3 Micromagnetic simulations

Magnetic states in ferromagnetic structures at the small scale varies with their geometry. We characterize and model the formation of magnetic states as a function of geometry using micromagnetic object oriented micromagnetic framework (OOMMF) simulations. With selective magnetic states, we use a fully coupled finite element analysis model to predict the magnetoelastic coupling in multiferroic heterostructures.

Both of the two simulations calculate the equilibrium magnetization based on Landau-Lifshitz-Gilbert (LLG) equation. The LLG equation is a differential equation that describes the dynamics of magnetization in a magnetic structure, which is given as

$$\frac{\partial \vec{M}}{\partial t} = -\mu_0 \gamma \vec{M} \times \vec{H}_{eff} + \alpha \left(\vec{M} \times \frac{\partial \vec{M}}{\partial t} \right) \tag{4}$$

where μ_0 is the permeability of free space, γ is the Gilbert gyromagnetic ratio, α is the Gilbert damping constant, and $\vec{M}$ is the normalized magnetization. The effective magnetic field, $\vec{H}_{eff}$, includes contributions from the external field ($\vec{H}_{ext}$), exchange field ($\vec{H}_{ex}$), demagnetization field ($\vec{H}_d$), and magnetoelastic field ($\vec{H}_{me}$) effects. It should be noted that due to the negligible magnetocrystalline anisotropy in polycrystalline magnetic materials, the magnetocrystalline anisotropy field is ignored in the effective magnetic field.

1.3.1 Object Oriented MicroMagnetic Framework (OOMMF)

OOMMF is used to study the geometric dependent formation of magnetic states in micro magnetic structures [32]. OOMMF determines the equilibrium magnetization of an object by locally and globally solving the LLG equation at distinct locations along a three-dimensional meshed grid of magnetic structures. The magnetization of each unit cell has three degrees of freedom. Additionally, the exchange stiffness constant, A, and the saturation magnetization, M_s, are specified in the modeling. Simulating a saturating magnetic field along one lateral axis saturates the magnetization in the structures. When the field is removed, the magnetic state evolves by an energy minimization process until the equilibrium state is achieved. We consider only exchange and demagnetization energies in the total magnetic energy and ignore the effect of magnetocrystalline energy. The magnetocrystalline anisotropy energy in polycrystalline magnetic materials, which is the case for this study, is relatively negligible compared to other energy terms.

1.3.2 Finite element analysis of magnetoelastic coupling

We use the numerical method[33] based on finite elements to fully-couple micromagnetic simulations with elastodynamics in finite size 3D structures. The weak forms of micro-magneto-electro-mechanical coupled equations are solved using finite element methods with an implicit backward differentiation formula (BDF) time stepping scheme. In order to decrease solution time, the system of equations with the dependent variables is solved using a segregated solution approach, which splits the solution process into sub-steps using a damped Newton's method. For all numerical problems, convergence studies (*i.e.*, mesh size and time steps) were evaluated to ensure accuracy. The element size was chosen to be comparable to the exchange length and the substrate and air were considered in the analysis. This coupled model provides an approach to simultaneously solve the full strain and micromagnetic spin distribution in the composite system as a function of position and time.

In order to adequately predict the magnetization states of the ferromagnetic ring structures as a function of electric field, it is necessary to model the magnetization dynamics using the LLG equation along with the mechanical stresses and strains *via* the equations of elastodynamics in the rings. For the substrate on which the rings are deposited, a piezoelectric model accounts for electric field effects using a quasi-static electric field approximation and for displacement phenomena with the elastodynamics equations. The electrostatic assumption only eliminates coupling with magnetic field components and does not limit the applicability of this model to predict the dynamic response presented in this paper.

The theoretical framework for this problem reduces to seven coupled partial differential equations (PDEs) that solve for magnetization, displacement, and magnetic potential in the

ferromagnetic rings and four coupled PDEs for the displacement and electric potential in the piezoelectric substrate. Modeling assumptions include small elastic deformations, linear elasticity, magnetostatics, electrostatics, and negligible electrical current contributions. The governing elastodynamic equations are

$$\rho \frac{\partial^2 \vec{u}}{\partial t^2} - \nabla \cdot \boldsymbol{\sigma} = \vec{0} \tag{5}$$

where ρ is the density, $\boldsymbol{\sigma}$ is the stress tensor, $\vec{u}$ is the displacement vector, and t is time. The LLG micromagnetic relation in Equation (4) represents the second set of equations

The quasi-static Ampere's law is $\vec{H}_d = -\nabla \phi_m$ where $\vec{H}_d$ is the demagnetization field vector and ϕ_m is the magnetic potential. This factor contributes significantly to the dipole-dipole coupling and the effective field in the LLG equation. Combining this equation with the divergence of magnetic induction equal to zero and the constitutive relation, $\vec{B} = \mu_0 (\vec{H} + \vec{M})$, produces an equation for ϕ_m in terms of the magnetization $\vec{M}$. The magnetization couples with the effective magnetic field through this demagnetization term. Further, substituting the constitutive relations into the elastodynamics and LLG equations produces a cross-coupled set of non-linear equations relating the displacements, the magnetization, and the magnetic potential as follows:

$$\rho \frac{\partial^2 \vec{u}}{\partial t^2} - \nabla \cdot \boldsymbol{C} \left[\frac{1}{2} (\nabla \vec{u} + (\nabla \vec{u})^T) \right] + \nabla \cdot \boldsymbol{C} (\lambda^M \vec{M} \vec{M}^T) = \vec{0} \tag{6}$$

$$\frac{\partial \vec{M}}{\partial t} = -\mu_0 \gamma \left(\vec{M} \times \left(\vec{H}_{ext} + \vec{H}_{ex}(\vec{M}) + \vec{H}_d(\phi_m) + \vec{H}_{anis}(\vec{M}) + \vec{H}_{me}(\vec{M}, \vec{u}) \right) \right) + \alpha \left(\vec{M} \times \frac{\partial \vec{M}}{\partial t} \right)$$

$$\tag{7}$$

$$\nabla^2 \phi_m = M_s (\nabla \cdot m) \tag{8}$$

where $\boldsymbol{C}$ is the stiffness tensor and λ^M is the magnetostriction tensor.

In a similar fashion to the magnetic potential, the quasi-static Faraday's Law implies that $\vec{E} = -\nabla\varphi_E$, where $\vec{E}$ is the electric field and φ_E is the electric potential. This equation coupled with Gauss's Law and a proper constitutive form provides for piezoelectric coupling within the model. COMSOL is used to solve the weak form of these systems of partial differential equations. This multiphysics solution produces point wise values for the mechanical displacement, electric potential, magnetic potential, and magnetization throughout multiferroic heterostructures.

1.4 Magnetic characterization techniques

There are various metrological techniques to measure nano- and micro- magnetization (Table 2). The magnetic characterizations can be classified into two types: invasive and non-invasive measurements.

The invasive measurements include superconducting quantum interference device (SQUID), vibrating sample magnetometer (VSM), and magnetic force microscopy (MFM). These are not able to visualize or image the orientation of magnetization. However, MFM is able to indirectly image magnetization using magnetic interaction between magnetic stray field from the sample and a magnetic tip on the tool. SQUID, and VSM are able to measure M-H curves with an external electromagnet.

Magneto-optical Kerr effect (MOKE), X-ray magnetic circular dichroism-photo emission electron microscopy (XMCD-PEEM), Lorentz transmission electron microscopy (Lorentz TEM), and scanning electron microscopy with polarization analysis are metrologies that provide direct imaging of magnetism. Except MOKE, for which resolution is limited by light diffraction, the

resolution of the direct techniques can resolve tens to hundreds of nanometers. However, they require sophisticated systems, such as sources of fine X-rays or fine electron beams.

In this work, we use MFM and XMCD-PEEM to study magnetism in the multiferroic heterostructures.

Table 2 Magnetic characterization techniques.

Type	Name	Source	Resolution	Measuring
Invasive measurements	SQUID	Electromagnet + superconducting loop with 2 Josephson junctions	~ 5 μ Oe	M-H loop
	VSM	Electromagnet + voltage pickup coil	~ 0.5 μ emu	M-H loop
	MFM	Stray magnetic field emitted from a magnetized tip	A few nanometers	Magnetic contrast images
Non-invasive meaurements	MOKE	Linearly polarized light	~ 1 μm	M-H loop, magnetic contrast images
	XMCD-PEEM	Polarized X-rays	Tens of nanometers	Planar magnetic contrast images
	SEMPA	E-beam	10 ~ 50 nm	Quantitative magnetization in the x, y, and z axis
	Lorentz TEM	E-beam	~ 10 nm	Distribution of transmitted electrons that are affected by Lorenz force

1.4.1 Magnetic force microscopy

Magnetic force microscopy is one of the scanning probe microscopy (SPM) techniques that scans the surface of a sample with a magnetized tip and measures the magnetic interaction between the tip and the stray field coming from the sample. Basically, the MFM tip is mounted on a piezoelectric holder and oscillates at its resonant frequency. A laser beam reflects off the surface of the tip to a photodiode detector that measures the response of the tip. By scanning the tip over the surface of a sample, the photodiode detects shifts in phase (phase detection mode), resonant frequency (frequency modulation mode), or oscillation amplitude (amplitude mode) caused by magnetic interaction between the tip and the sample. The shifts are used to construct magnetic structures in the sample. The schematic of MFM is shown in Figure 2a.

MFM can easily visualize simple submicron scale magnetic structures, such as magnetic single-domain as shown in Figure 2c. However, since MFM only senses the stray field from a sample, not direct magnetizations of the sample, it is an indirect measurement. Therefore, it is not suitable for imaging complex magnetic structures. Also, MFM might cause an undesired change in the sample due to the magnetic field emanating from the tip.
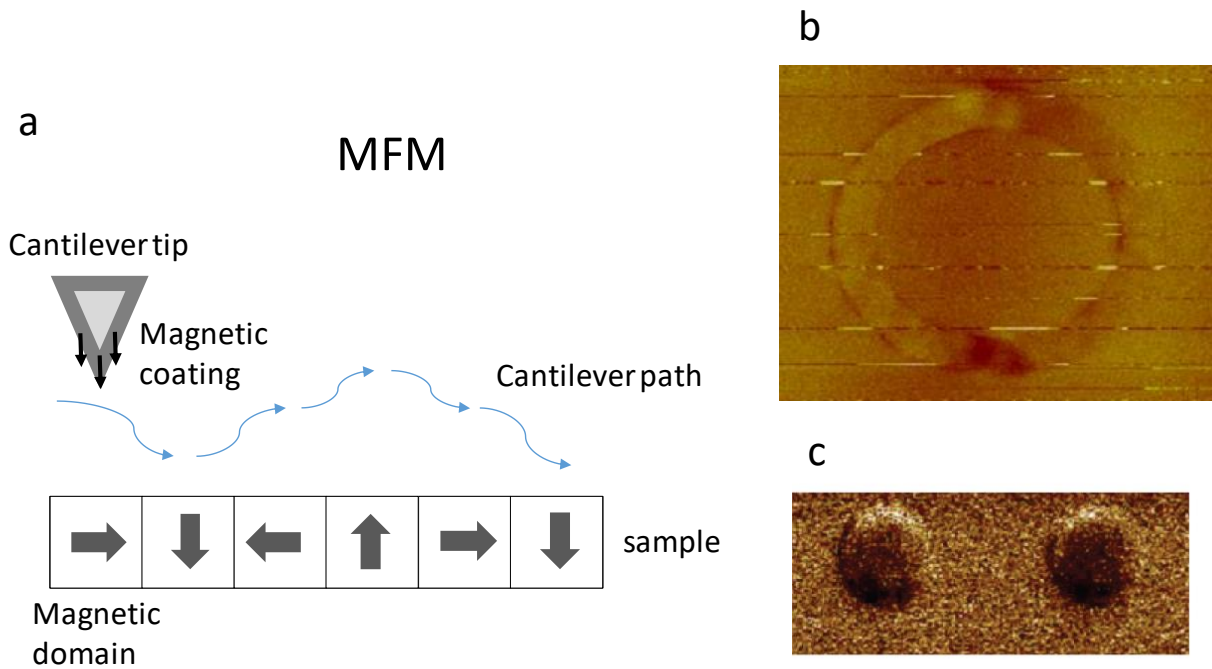
Figure 2 Schematic of MFM and its images (a) Detecting magnetic interaction between the stray field from the sample and the magnetic tip (b) MFM image of 1 μm Ni rings forming magnetic domain at the top and bottom. (c) MFM image of a magnetic single-domain in 400 nm Ni disks.

1.4.2 X-ray magnetic circular dichroism-photo emission electron microscopy

X-ray magnetic circular dichroism-photo emission electron microscopy (XMCD-PEEM)[34, 35] is a direct measurement of the magnetization in a sample. In XMCD-PEEM, two opposite circularly polarized x-rays have different x-ray absorption spectra depending on the magnetization direction in a sample. This difference in x-ray absorption maximizes when the X-ray energy is tuned at the $L_{2,3}$ absorption edges for the 3d transition metals such as Fe, Co, and Ni. When the X-rays are absorbed by the sample, 2p electrons are excited to unfilled states in 3d level which bears magnetic configuration. By following Auger processes and inelastic electron scattering, secondary electrons that hold the spin and orbital moments are emitted from the

sample to vacuum and collected by the PEEM optics. The PEEM optics analyze the collected electrons and image nanoscale magnetizations. Depending on the magnetization direction in the sample with respect to the X-ray propagation direction, the PEEM optic generates magnetic contrast. Magnetization that is parallel to the X-ray propagation direction appears either black or white, and magnetization that is normal to the X-ray shows gray. The several PEEM images are shown in Figure 3. In Figure 3a, b, the magnetic states have a magnetic flux closure form and are observed as a circular color gradient. In addition, magnetic onion state, which has two half circular magnetizations heading toward one direction, is shown in Figure 3c.

The resolution of XMCD-PEEM can go down to 30 nm spatial resolution [36]. However, it requires fine X-ray sources, which typically are generated by a synchrotron. Therefore, access to XMCD-PEEM is limited. Some of the facilities with XMCD-PEEMs are Advanced Light Source in Lawrence Berkeley Lab, USA; Swiss Light Source in Paul Scherrer Institut, Switzerland; SOLEIL in Paris, France; BESSY II in Helmholtz Zentrum Berlin, Germany.
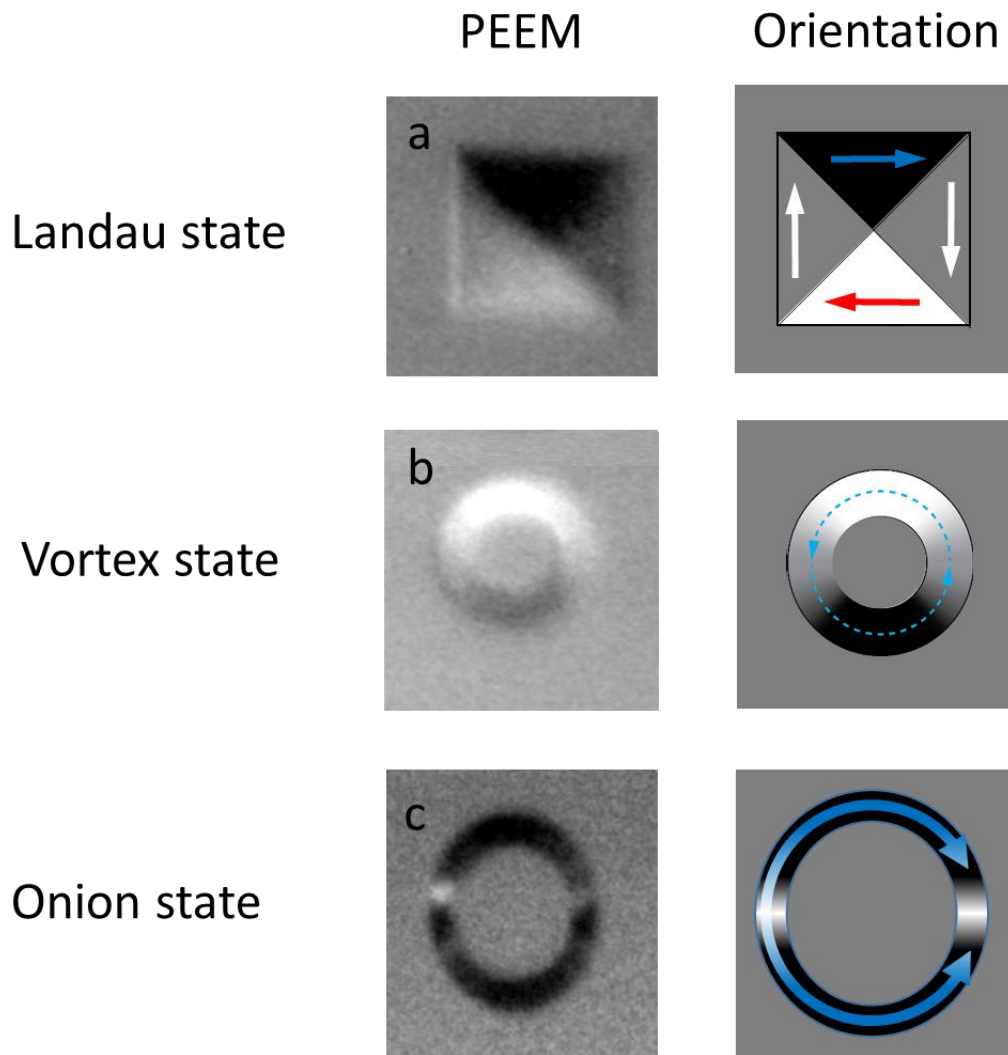
Figure 3 XMCD-PEEM images of Ni microstructures (a) 2 μm x 2 μm Ni square showing Landau closure state (b) 2 μm outer diameter (OD)/1 μm inner diameter (ID) Ni ring presenting vortex state; (c) 2 μm OD/ 1.4 μm ID Ni ring demonstrating magnetic onion state.

CHAPTER 2
NICKEL THIN FILM MICROSTRUCTURES

2.1 Magnetostrictive material: Nickel

Ni belongs to the 3d-transition metal group and exhibits ferromagnetic properties at room temperature. Saturation magnetization of Ni is 486 emu/cc, exchange stiffness, 9 x 10^{-12} J/m, and exchange length, 7.72 nm. Ni behaves like a paramagnetic material above its Curie temperature, 355°C. Ni is also known for a magnetostrictive material. Its magnetostriction constants are

$$\lambda_{100} = -46 \times 10^{-6} \text{ and } \lambda_{111} = -25 \times 10^{-6}$$

$$\lambda_s = -34 \times 10^{-6}$$

where λ_{100} and λ_{111} are the magnetostriction constant in [100] and [111] directions, and λ_s is the saturation magnetostiction. This implies that Ni contracts in the direction of magnetization for any direction. By inverse magnetostrictive effect, magnetization in Ni also changes its preferred directions with an applied strain, favoring a contraction.

Among many magnetostrictive materials, thin film Ni is chosen in this study for initial characterization of magnetoelastic coupling behavior. Ni has a decent magnetostriction, creating an easy axis along compressive strain. In addition, unlike other metal alloys, Ni is relatively easy to process and fabricate.

2.2 Magnetic states in thin film structures

Magnetic thin film structures possess interesting properties. Since out-of-plane magnetization is restricted by its high demagnetization factor, magnetic anisotropy is mostly favorable in-plane. Because of the fewer degrees of freedom, control of magnetization in thin film structures is predictable and deterministic, which are very important in many applications such as magnetic storage, magnetic spintronics, and magnetic sensors.

At the macro scale, magnetic structures are mostly in multi-domain states. At the micro- and nanoscale, forming multi-domains comes with higher exchange energy cost, and thin film structures start to possess more uniform magnetizations. In magnetic ring structures, magnetic "onion" state and vortex state are observable. In magnetic disk and ellipse structures, homogenous magnetic domain, a magnetic single-domain state, is created and emits stray field like a bar magnet. These magnetic states can be useful because they can store a bit data and has ability to interact with external magnetic particles.

2.3 Magnetic states in Nickel ring structures

Ferromagnetic ring elements have been studied for their symmetric shape (yielding well-defined and stable magnetic states), as well as their varied magnetic states[37]. At the large scale (feature size > 4 μm), magnetic states in ring structures show multi-domain states (Figure 4c). One interesting magnetic state available to the ring geometry is the magnetic "onion" state, which is observed at the micron- or submicron-scale (Figure 3c and Figure 4b). A remnant onion state can be formed under certain geometric and material constraints by applying a saturating

magnetic field along an in-plane direction and then releasing the applied field[38]. The onion state possesses two opposite circular magnetizations, and their direction depends on the previous magnetization process. Due to its ability to maintain a magnetic state with no applied field, a few studies have attempted to manipulate the onion state for possible application in magnetic memory[39]. Reorientation of the onion state requires energy to overcome an energy barrier at its energy minimum[18].

Another state that is observed with the onion state is the vortex state (Figure 3b and Figure 4a). This vortex state is observable in the ring structures with wider width. However, due to its closure form of magnetization, it has very small magnetic energy to emit any stray field, or to interact with outer environment. Therefore, in this study, we limit our scope to the characterization and control of onion state.

a

Vortex state

Scaling down

b

Onion state

c

Multi-domain states
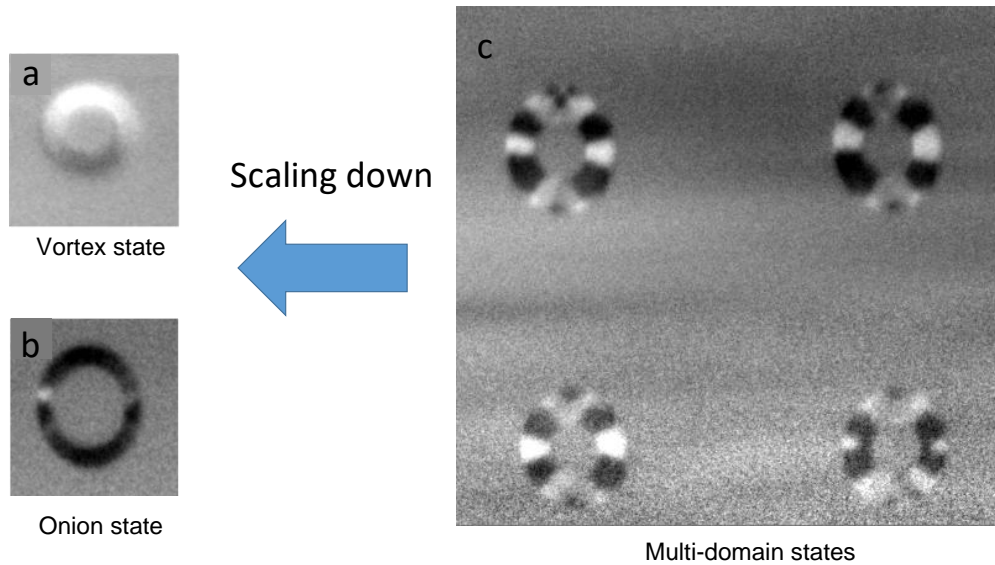
Figure 4 PEEM of magnetic states in Ni ring structures with different geometries. (a) Magnetic vortex state in a Ni ring with 2.0 μm outer diameter(OD)/1 μm inner diameter(ID). (b) Magnetic onion state in a Ni ring with 2.0 μm OD/ 1.4 μm ID. (c) Magnetic multi-domain states in Ni rings with 4.0 μm OD/ 2.0 μm ID

2.3.1 Characterization

To reliably obtain an onion state, we first characterize and model the formation of onion state as a function of ring geometry both experimentally and with conventional micromagnetic OOMMF simulations[32]. Using electron-beam lithography, we fabricate a number of ferromagnetic Ni rings (15 to 45 nm thick) with outer diameters (OD) ranging from 1 µm to 2 µm while systematically varying the ring widths (W) from 650 nm to 150 nm. XMCD-PEEM [34, 35] is used to obtain magnetic contrast images of the ring structures.

Prior to PEEM imaging, each magnetic ring sample is initialized with a 3 kOe external magnetic field, which is sufficiently large to saturate magnetization in Ni, to create an onion state. The stability of the onion state upon removal of the initialization field depends on the ring dimensions[40]. OOMMF micromagnetic simulations[32] were used to calculate the minimized magnetic energy density as a function of the W/OD ratio after initialization in 30 nm thick rings with an OD of 1.0, 1.5, 2.0, and 4.0 µm (Figure 5a) and in 15 nm thick rings with an OD of 1.0 and 2.0 µm (Figure 5b). For the 30 nm thick rings (Figure 5a) we observe three distinct energy density minima regimes with decreasing W/OD for each OD value: 1) the vortex state (*i.e.* where the ring magnetization is circularly oriented along the circumference with no domain walls) in the bottom right corner (shaded in green) representing the lowest total energy density on the plot, 2) the onion state in the middle of the figure (not shaded) that contains vortex-like domain walls, and 3) the onion state in the upper left of the figure (shaded in blue) which contains transverse-like domain walls and has the largest total energy density.

Figure 5c-e show XMCD-PEEM images while Figure 5f-h show simulated micromagnetic images for 30 nm thick, 2 µm OD rings with widths varying from 200 nm to 650 nm following initialization (as indicated on Figure 5a). The exchange (favoring parallel domains

and local alignment of the magnetization) and demagnetization (favoring closure domains and minimization of the stray magnetic fields) energies are the dominant contributions to the total energy shown in Figure 5a and these compete to rearrange the micromagnetic magnetization properties of the Ni rings into the lowest accessible energy state as indicated by the three regions of Figure 5a. In the initialized state, there is a high local energy density associated with the ends of the onion state where the magnetization vector fields point towards a ring wall (a large demagnetization component). The redistribution of this high local energy density, upon removal of the external 3 kOe magnetic field, is dependent upon the W/OD parameters of the ring. The gradient of the local energy density relative to the energy density of a slightly perturbed magnetization configuration represents the driving force on the magnetization causing it to move to a stable or metastable state (*i.e.* if a slightly different magnetization configuration than the current state has lower energy, the system experiences a force pushing it toward the new state). The large initial demagnetization energy in wider rings dominates the exchange energy component driving the ring into the vortex state (Figure 5e and h and bottom right of Figure 5a). This vortex state forms because the demagnetization energy required to rotate the magnetization 180° for a wide ring is relatively low compared to the exchange energy. The high local energy density of the initialized state can overcome the local exchange energy barrier and the magnetization along one half of the ring flips direction producing a vortex ring state.

As the ring width narrows, the demagnetization energy required to rotate the magnetization 180° becomes higher. This causes the perturbation states associated with rotating the magnetization past a wall to be relatively high. As the ring width narrows to approximately W/OD = 0.3 the driving force supplied by the demagnetization energy to rotate the magnetization no longer overcomes the exchange energy and extrinsic domain wall pinning due

to edge roughness leaving the ring in an onion state once the field is removed (Figure 5c, d, f, g). The high energy density tends to redistribute into a local vortex domain wall. As the W/OD ratio decreases further, the gradients between neighboring states continues to decrease and the onion state itself becomes metastable (*i.e.* two possible domain wall types: vortex and transverse). While these simulations show a transition between the domain wall type (vortex to transverse domain wall) as a function of the ring geometry, they do not account for thermal effects which can influence the nature of the domain walls at room temperature[41]. This, coupled with the fact that the PEEM resolution limits our ability to identify the precise type of domain walls we obtain in thinner rings that are 30 nm thick, means we cannot conclusively state where the precise vortex to transverse domain wall transition occurs. Nevertheless, the simulations shown in Figure 5a are in qualitative agreement with our PEEM imaging measurements and the results confirm stable onion states are achievable in 30 nm thick Ni rings with W/OD ≤ 0.3 as identified by the model in Figure 5a.

The OOMMF simulations[32] of the 15 nm thick rings (Figure 5b) do not show a W/OD dependence between onion states and vortex states in either the 1 µm or 2 µm OD rings up to a W/OD of 0.4. Instead, in all cases an onion state with transverse domain wall type is observed. These thinner rings are exchange dominated and do not possess the requisite demagnetization energy required to flip the magnetization direction radially past a ring wall. From Figures 2a and 2b we find that the properties of the onion states are dependent on the ring thickness[42] with thinner rings having a higher probability to form transverse domains (Figure 4c, f). Our OOMMF model confirms a previous study[43] that found transverse domains produce stray magnetic fields with larger magnitudes as indicated by the higher energy densities.

a Thickness 30 nm

b Thickness 15 nm

Onion state
Onion state Transverse DW
Transverse DW
Simulation
1.0 µm
1.5 µm
2.0 µm
4.0 µm
Onion state
Vortex DW
Vortex State
Simulation
1.0 µm
2.0 µm
Onion state
Transverse DW

Onion state **Onion state** **Vortex state**

PEEM image

Simulation

+M_y
-M_x
+M_x
-M_y

Magnetization contrast

OD:	2.0 µm	2.0 µm	2.0 µm
W:	200 nm	300 nm	650 nm
W/OD:	0.100	0.150	0.325
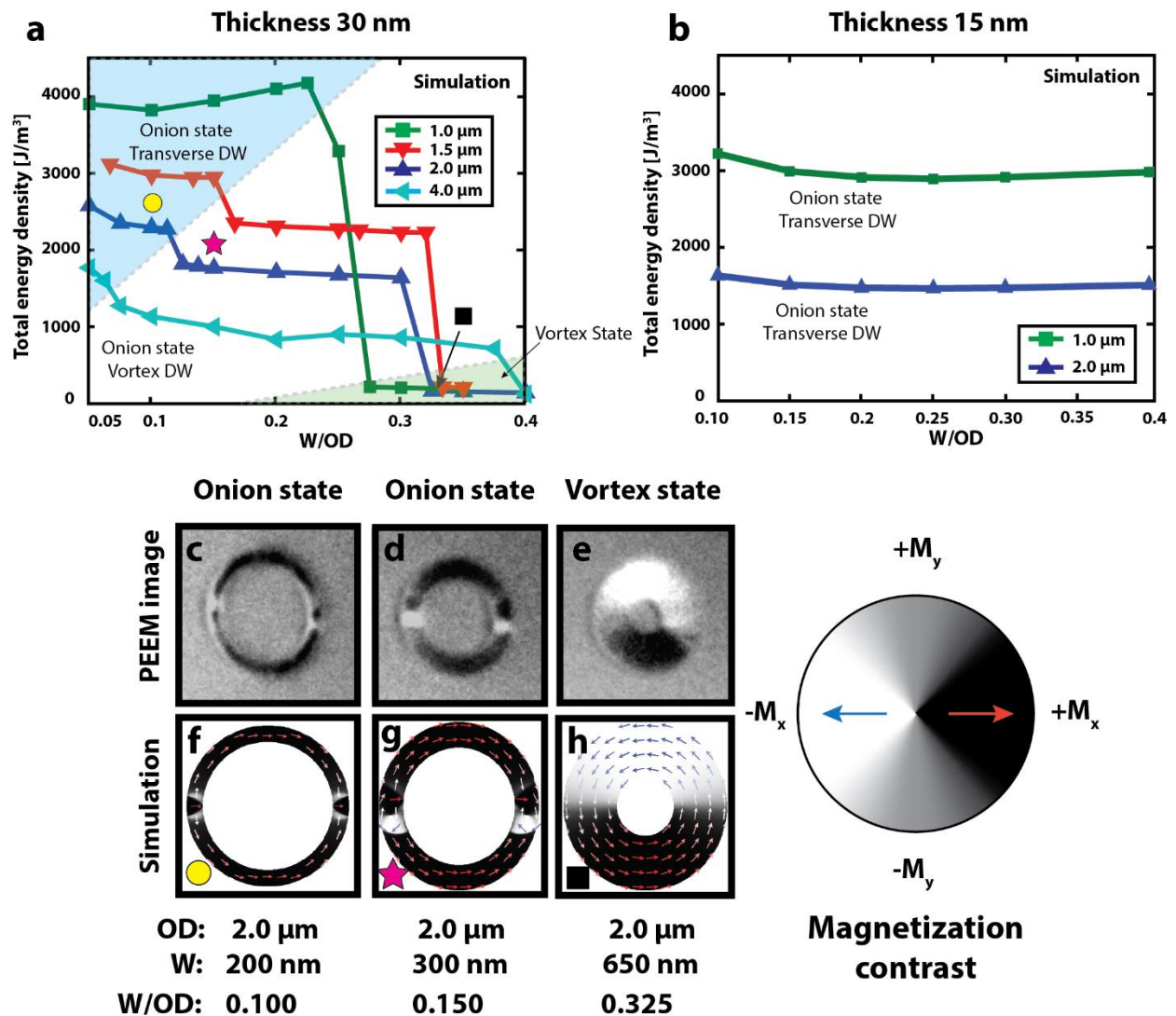
Figure 5 Initializing a stable onion state (a,b) The total energy density (assuming room temperature constants) calculated from micromagnetic simulations of (a) 30 nm thick, 1, 1.5, 2, and 4 µm OD rings and (b) 15 nm thick, 1 and 2 µm OD rings as a function of W/OD after the application and removal of a 3 kOe field in the absence of a thermal environment. In (a) the three distinct regions (highlighted in green, white, and blue) correspond to the three possible initialized magnetization states: a vortex state, an onion state with vortex domains, and an onion state with transverse domains. Dashed lines are a guide to the eye. (c-e) XMCD-PEEM images taken at room temperature of 30 nm thick, 2 µm OD rings with widths of 200, 300, and 650 nm, respectively. (f-h) Complementary micromagnetic simulations for rings with identical geometries in parts (c-e). Black and white contrast orientation is identical to PEEM images and the red and blue colored arrows indicate the magnetic orientation of individual grid elements from the micromagnetic simulation. The yellow circle, pink star, and black square indicate where each simulated geometry (and W/OD ratio) is located on the graph in part (a).

2.4 Magnetic states in Nickel disk structures

In a similar way as Ni ring structures, Ni disk structures create multi magnetic domains at the micron scale. SD states in thin film ferromagnetic disks are achievable when the devices are scaled to sub-micron length scales (Figure 6). The critical size to form a SD state depends on the exchange length, saturation magnetization, and shape anisotropy of the material. For a 15nm thick Ni disk, a SD state starts to form in disks with diameter less than 400 nm[44]. The SD state in thin film disks possesses several useful properties for magnetic applications. First, due to its homogeneous configuration of magnetization, the magnetic single-domain emits a stray magnetic field at opposing sides of the disk, creating a dipole field for interaction with the external environment (Figure 6). Second, the ferromagnetic structures have non-volatile, spontaneous magnetization, which can serve as a constant magnetic source. In addition, due to its symmetric circular shape, the disk structure does not possess shape anisotropy in the azimuthal angle or any preferential easy axis in-plane. Therefore, we can achieve isotopic rotation of SD states in the disks.

The magnetic energies that influence the SD state in the Ni nanodisks are the magnetocrystalline energy, exchange energy, demagnetization energy, and magnetoelastic energy. In this study, Ni disks are deposited by electron-beam evaporation and form polycrystalline structures, which means the macroscopic magnetocrystalline anisotropy energy is negligible compared to the other energy terms[45]. Therefore, creation of a magnetic SD state in Ni disks can be determined by an energy minimization process and balance between the exchange energy and demagnetization energy. After applying a saturating magnetic field, the initial homogeneous magnetization in disk structures produces a large internal demagnetization

field that tends to create multi-domains or a vortex state to reduce the large demagnetization energy, which comes with increase of the exchange energy. Below a certain size scale, the exchange energy dominates the demagnetization energy, reducing the favorability to form multi-domain states.

Figure 6 shows the magnetic SD state in a Ni disk with 15 nm thickness and 400 nm diameter using OOMMF. Near the edge of the disk where the magnetic field comes in and out, the magnitude of maximum magnetic field shows 2.8 kOe. This is sufficiently high to interact with outer environment, such as magnetic particles.
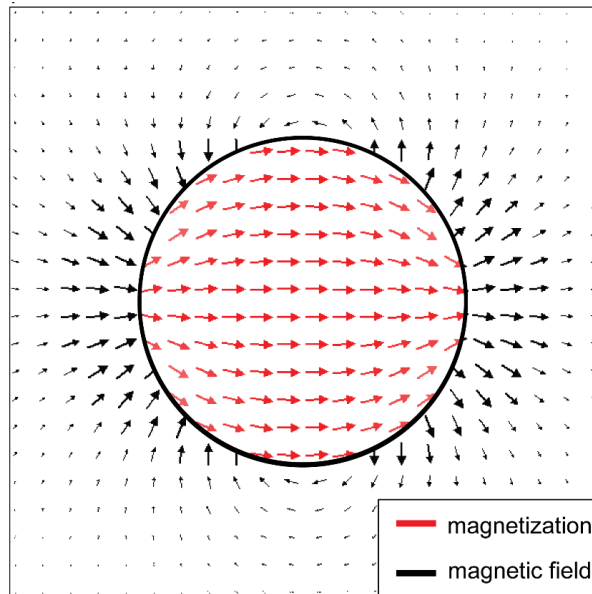
Figure 6 Magnetic single-domain state in a Ni disk with thickness of 15nm and diameter of 400 nm The result is obtained by Object Oriented MicroMagnetic Framework[32] (OOMMF). Saturation magnetization M_s= 485 emu/cc, and exchange constant A= 9.0 x 10-12 J/m are used in the simulation, and the disk emits maximum stray magnetic field of $|H_{max}|$=2.8 kOe.

2.5 Control of magnetization in thin Ni structures with mechanical strain

By applying strain to magnetization, we can reshape the energy landscape through control of the magnetoelastic energy. For polycrystalline thin film structures, we can assume in-plane isotropic magnetoelastic energy, given as

$$E_{m.e.} = -\frac{3}{2}\lambda_s E\left(s_x \cos^2\theta + s_y \sin^2\theta\right) = -\frac{3}{2}\lambda_s E\left[\left(s_x - s_y\right)\cos^2\theta + s_y\right] \qquad (6)$$

, where λ_s is saturation magnetostriction, E is Young's modulus, θ is the angle between magnetization and strain, and s_x and s_y are strain in x, and y, respectively (Figure 7a). If the applied strain provides sufficient energy to overcome the local energy barrier that is imposed by the current exchange energy and demagnetization energy, the magnetization will realign toward the new easy axis formed by the strain. To more effectively drive the SD states, we calculate the optimal control angle to apply a strain with respect to a magnetic single-domain. This is found by the magnetoelastic effective field,

$$\vec{H}_{m.e.} = -\frac{1}{\mu_0}\nabla E_{m.e.} = \frac{1}{\mu_0}\frac{1}{r}\frac{\partial}{\partial\theta}(-\nabla E_{m.e.})\hat{\theta} = -\hat{\theta}\frac{3}{2}\frac{1}{\mu_0}\frac{1}{r}\lambda_s E\left(s_x - s_y\right)\sin 2\theta \qquad (7)$$

This effective field is the local field that the disks experience due to the applied strain. The magnetic effective field is a function of $\left(s_x - s_y\right)$ and $\sin 2\theta$. The maximum magnitudes of the field are at ±45°, or ±135°. In addition, the effective field can be increased by a larger strain difference, $\left(s_x - s_y\right)$. Therefore, applying different polarity of orthogonal strains with $\left(s_x s_y < 0\right)$ at +45° or -45° toward a magnetic single-domain maximizes the initial effective field that help overcome the local energy barrier and reorient the magnetization toward the new easy axis. For example, the magnetoelastic energy and magnetoelastic effective field for $\left(s_x - s_y\right) < 0$ and

$\lambda_s < 0$ are shown in Figure 7b. In this case, the minimum $E_{m.e.}$, or easy axis, is created along the x axis, and the maximum effective field is generated when magnetization with $\theta = \pm45°, \pm135°$.
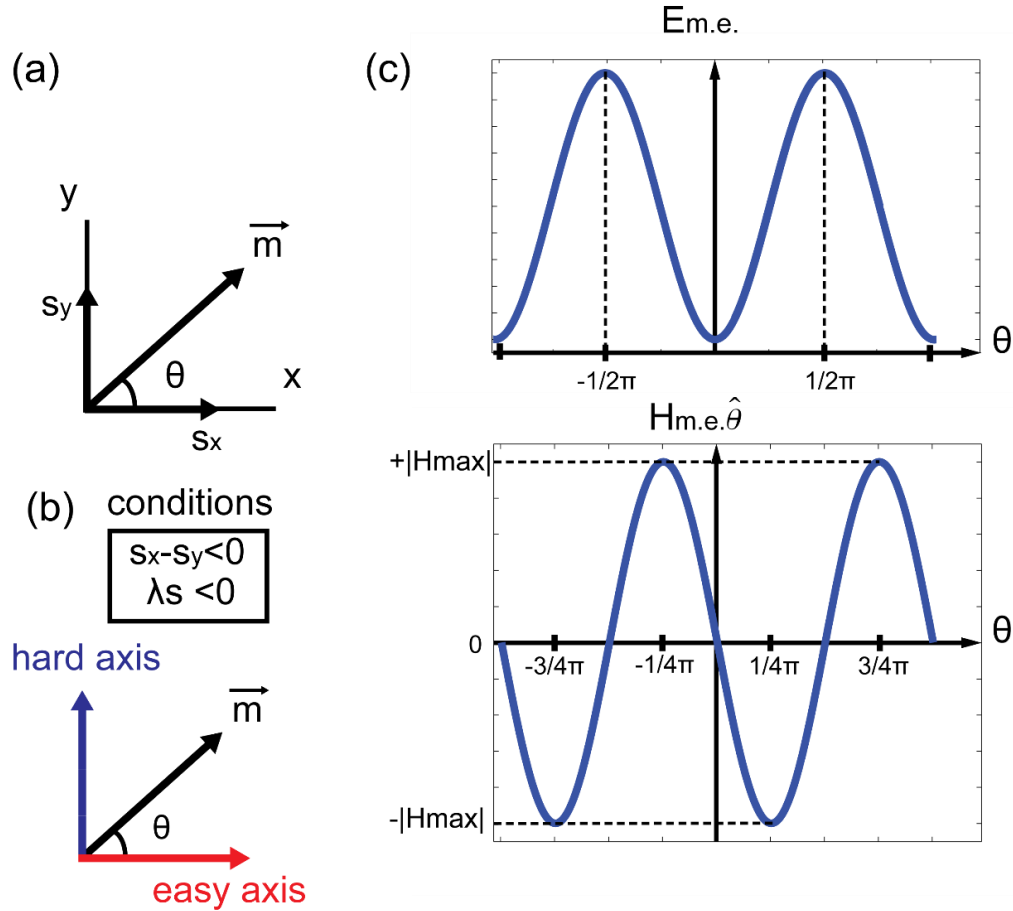
Figure 7 Calculation of the optimal angle to apply strain toward magnetization (a) Orientations of strain and magnetization (strain in x, s_x, strain in y, s_y, magnetization, m, and angle between s_x and m, θ) (b) Orientations of the easy and hard axis when $(s_x - s_y) < 0$ and $\lambda_s < 0$. The easy and hard axis are created along the x and y axis, respectively (c) The magnetoelastic energy and magnetoelastic effective field for $(s_x - s_y) < 0$ and $\lambda_s < 0$. Magnetization at $\pm45°$ experiences the maximum effective field of $\mp|Hmax|\hat{\theta}$ toward the closest easy axis, the +x axis. If the magnetization was closer to the hard axis, away from $\pm45°$, the effective field decreases. At $\pm90°$ (i.e., the hard axis), and the magnetization is in a metastable equilibrium state. The magnetization at the hard axis rotates either clockwise or counter-clockwise with a small disturbance, which makes rotation non-deterministic.

CHAPTER 3

CONTROL OF MAGNETIZATION USING PMN-PT SUBSTRATES

3.1 PMN-PT-based multiferroic heterostructures

Single crystal lead magnesium niobate-lead titanate, $[Pb(Mg_{1/3}Nb_{2/3})O_3]_x$ -$[PbTiO_3]_{(1-x)}$ (PMN-PT, $x \cong 0.34$ in this study) is known to exhibit a high piezoelectric effect. Unlike piezoelectric ceramics, which are made of small grains and not efficient to respond to electric fields, PMN-PT is made of single crystal and generates large piezoelectric strain with response to an applied electric field. This makes suitable piezoelectric materials to initially seek for the possibility to manipulate magnetization in magnetic structures.

In this work, [011]-cut PMN-PT bulk substrates are used to generate large in-plane strain. The strain curve in Figure 8 is measured using two strain gauges (Vishay EA-06-062AP-120) that are attached on the surface of a 500 µm thick PMN-PT substrate along the two major crystal directions, [011] and [011] directions. The polarity of d_{31} and d_{32} [011]-cut PMN-PT is opposite, generating anisotropic strain in-plane. With a 0.8 MV/m of electric field across the 500 µm thick PMN-PT, 1300 ppm of tensile strain in $[01\bar{1}]$ direction and -4000 ppm of compressive strain in [001] are generated (Figure 8).

We fabricate an array of ferromagnetic Ni rings with varying outer diameters (OD) and widths (W) on the surface of a Pt-coated (front and back) 500 µm thick PMN-PT substrate. The

Pt acts as an electrode for the PMN-PT substrate. XMCD-PEEM[34, 35] is used to obtain

magnetic contrast images of our multiferroic heterostructures (Figure 9b)
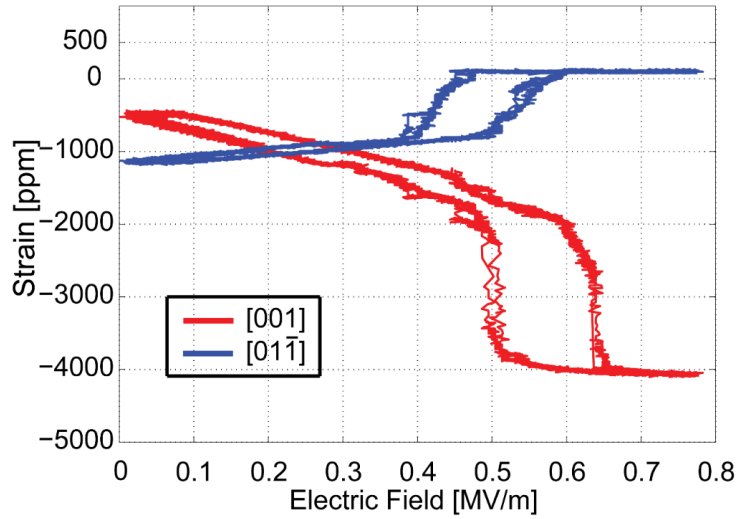
Figure 8 Strain curve of [011]-cut PMN-PT substrate measured with strain gauges
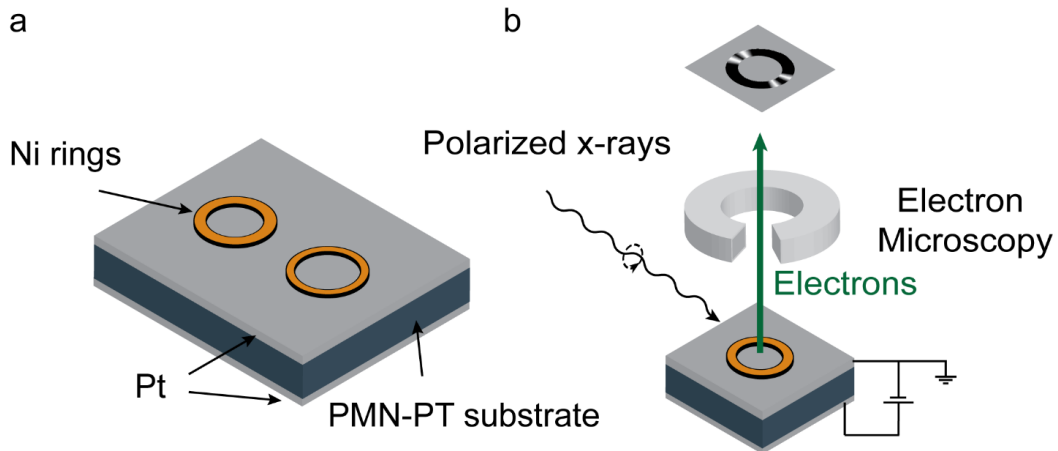
Figure 9 PMN-PT-based multiferroic heterostructure and experimental method, PEEM: (a) Schematic of a multiferroic heterostructure consisting of ferromagnetic Ni rings fabricated on the Pt-coated surface of a PMN-PT substrate. (b) The magnetic properties of the Ni rings are observed by XMCD-PEEM with an in-situ out-of-plane electric field applied across the substrate as indicated

3.2 Fabrication process

A 10 mm x 10 mm x 0.5 mm (011)-cut $[Pb(Mg_{1/3}Nb_{2/3})O_3]_{0.66}$-$[PbTiO_3]_{0.34}$ (PMN-PT from TRS Technologies) substrate is used as a piezoelectric material. On the top and bottom of the PMN-PT substrate, 5 nm Ti/50nm Pt (adhesion layer/electrode) is deposited by CHA electron-beam evaporator as shown in Figure 10a. A double layer of positive electron-beam resists (MMA EL-6/PMMA 950) is spun on the PMN-PT substrate for a lift-off mask (Figure 10b). As shown in Figure 10c, the double layer of the resists provides an undercut resist profile, which enable an easier lift-off process. Using electron-beam lithography, we pattern a number of ferromagnetic Ni rings (15 to 45 nm thick) with outer diameters (OD) ranging from 1 μm to 2 μm while systematically varying the ring widths (W) from 650 nm to 150 nm on the PMN-PT. Since the initial PMN-PT substrate has random orientation of polarization, initial poling process results in remnant polarization and strain. To eliminate the remanent strain in the Ni structures, the PMN-PT substrate is subjected to a 0.4 MV m^{-1} out-of-plane electric field prior to Ni deposition. Then Ni is evaporated on the Pt surface of the sample (Figure 10d). Following lift-off process with acetone solution, the Ni ring structures are on the PMN-PT substrate (Figure 10e). SEM images of fabricated Ni rings are shown in Figure 11.

(a) Deposition of Platinum	(b) Coat PMMA and MMA EL-6	(c) E-beam lithography and development
(d) Deposition of Ti/Ni	(e) Lift-off process	Ni PMMA MMA EL-6 Pt PMN-PT Pt
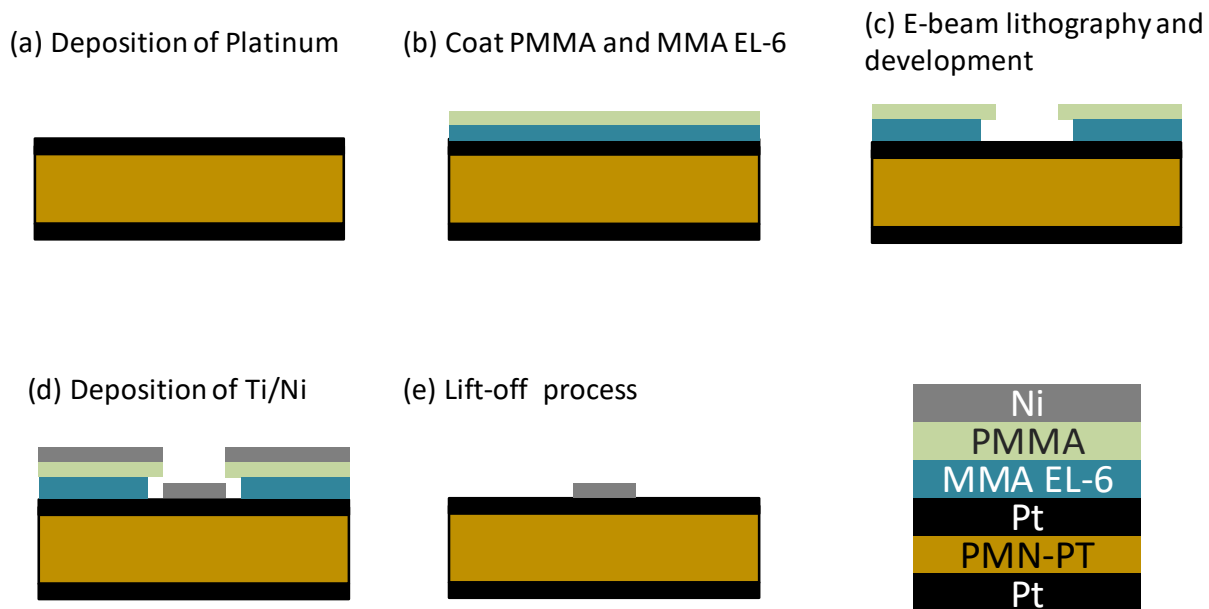
Figure 10 Fabrication process flow of Ni ring structures on a PMN-PT substrate
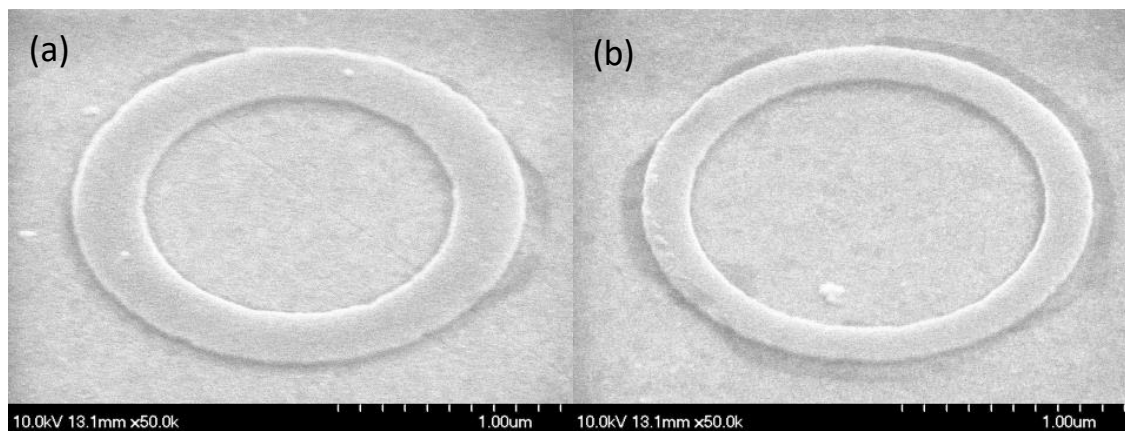
Figure 11 SEM of 30 nm thick Ni rings on a PMN- PT substrate. (a) A Ni ring with 2.0 μm OD and 1.4 μm ID. (b) A Ni ring with 2.0 μm OD and 1.6 μm ID

3.3 Experimental results

Selecting 30 and 15 nm thick Ni rings with W/OD < 0.3, we experimentally demonstrate deterministic rotation of domain walls by applying an electric field to the PMN-PT substrate. The rhombohedral single crystal PMN-PT used in this study has a spontaneous polarization along the <111> directions and the <011> cut of these substrates give large in-plane anisotropic strains upon application of an electric field across the substrate[25]. Based on previous works[17, 18, 46], the electric field induced strain in the piezoelectric substrate modifies the magnetoelastic energy component (H_{me}) of the Ni to create energetically favorable conditions that can reorient the domain walls toward the dominant compressive strain axis. Figure 13a shows the electric field induced strain in the poled PMN-PT sample characterized with a strain gauge along the in-plane [100] and [01$\bar{1}$] directions. A 0.8 MV m^{-1} electric field produces a 4000 ppm of compressive strain in the [100] direction and a 1300 ppm of tensile strain in the [01$\bar{1}$] direction (Figure 3b). The hysteretic strain jump at E ≈ 0.5 MV m^{-1} is a result of a morphotropic phase transition in the PMN-PT[47] sample but upon removal of the electric field the strain returns to zero. The applied anisotropic strain state should produce a rotation of the domain walls toward the [100] direction [18] due to the fact that Ni is a negative magnetostrictive material. In the following analysis and discussion, we assume the deposited Ni structures are initially unstrained.

XMCD-PEEM[34, 35] (Figure 9b) is used to obtain magnetic contrast images of the multiferroic heterostructures (Figure 9a). Figure 12 shows the 45° rotation of onion states with an electric up to 0.52 MV/m. The onion state started to rotate at 0.40 MV/m. The ring of 2.0 μm/ 1.4 μm exhibited a more significant change than the ring of 2.0 μm/ 1.6 μm, which started reorienting at 0.44 MV/m. The difference in magnetization between the two rings was attributed

to the ratio of the demagnetization energy to exchange energy. The ring with a wider width has a less in-plane demagnetization factor, which is easier to reorient magnetization. In addition, in the narrower ring, the domain wall pinning is severe due to a stronger interaction with edge roughness that plays a relatively larger role compared to the wider ring.
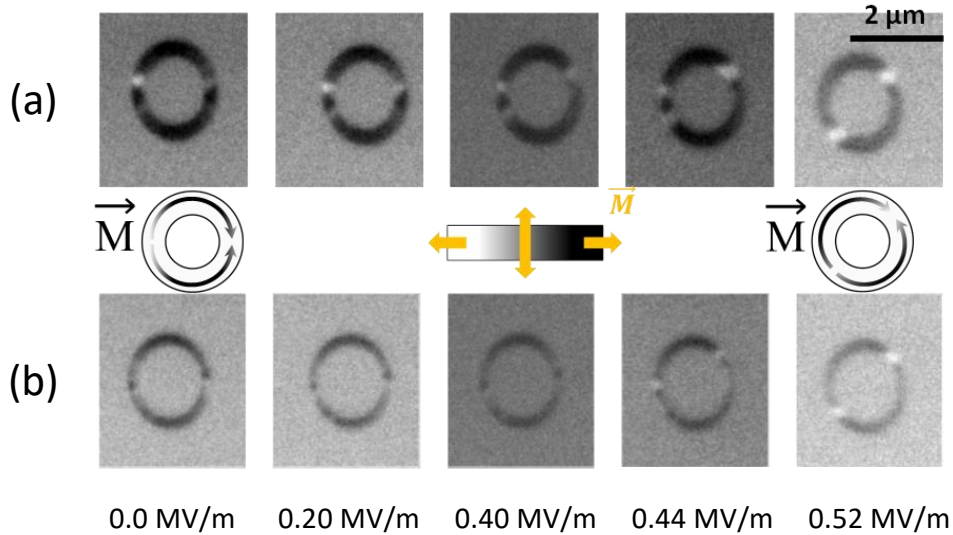
Figure 12 PEEM images of nickel rings with increasing E-fields. (a) A Ni ring with 30 nm thickness/ 2 μm OD / 1.6 μm ID (b) A Ni ring with 30 nm thickness/ 2 μm OD / 1.6 μm ID

Figure 13c-f show the XMCD-PEEM images of initialized onion states in a 2 μm OD, 300 nm wide and 1 μm OD, 150 nm wide ring for both 30 nm (Figure 13c,e) and 15 nm (Figure 13d,f) thicknesses, respectively. The simulated images in Figure 13 are solved with the coupled partial differential equations to determine the magnetization dynamics of the Ni ring geometries with respect to the electrical response of the piezoelectric substrate. Initially a 3 kOe external magnetic field is applied to each sample and simulation is initialized with an onion state at a 45° angle relative to the [100] strain axis as indicated in Figure 13b. We note that the resulting onion

state vortex domain walls have an equal probability of being clockwise or counter-clockwise oriented (compare Figure 13c and k), however this domain helicity does not impact the magnetic response due to strain. In the XMCD-PEEM study an image of the magnetic state of the rings is recorded at 0.04 MV m^{-1} intervals up to a maximum electric field of 0.8 MV m^{-1}. Near the critical electric field where the large strain jump occurs in Figure 13a, we observe a piecewise domain wall reorientation along the compressive [100] strain axis of the PMN-PT substrate indicated in Figure 13g-j for each ring respectively as compared to their initial states shown in Figure 13c-f. This electrically generated piecewise domain wall rotation is also predicted in the "simulated PEEM images" and their corresponding micromagnetic plots in Figure 13o-r and Figure 13w-z, respectively. The electrically-driven, strain-mediated domain wall rotation in the simulated Ni rings agrees well with our experimental observations.

For both the simulations and experiment, no further domain wall motion is observed at higher electric fields. The strain applied in the PEEM images is global and affects all the patterned structures on the surface. The behavior we see demonstrates a deterministic manipulation of the domain wall defined by the relative orientation of the initialized magnetization direction and PMN-PT strain axis. However, similar experiments where the domain walls were initialized 90° relative to the PMN-PT [100] axis showed little domain wall rotation response. In this case, clockwise and counterclockwise domain wall rotations are equally probable and experimental results for this initialization scenario have shown both a low tendency to rotate and an approximately equal CW and CCW rotation in rings where significant rotation is observed. Furthermore, micromagnetic/elastodynamic simulations of this case in a 30 nm thick, 2 µm OD, 300 nm wide ring reveals no significant rotation of the initialized domain walls with a strain of up to 10,000 ppm applied (more than twice the amount of strain we are experimentally

capable of applying). Instead new domain walls are formed along the PMN-PT [100] axis 90°

offset from the existing initialized domain walls when a strain of 5000 ppm is applied. In general,

we have found it is experimentally challenging to rotate the domains walls from a 90° offset.
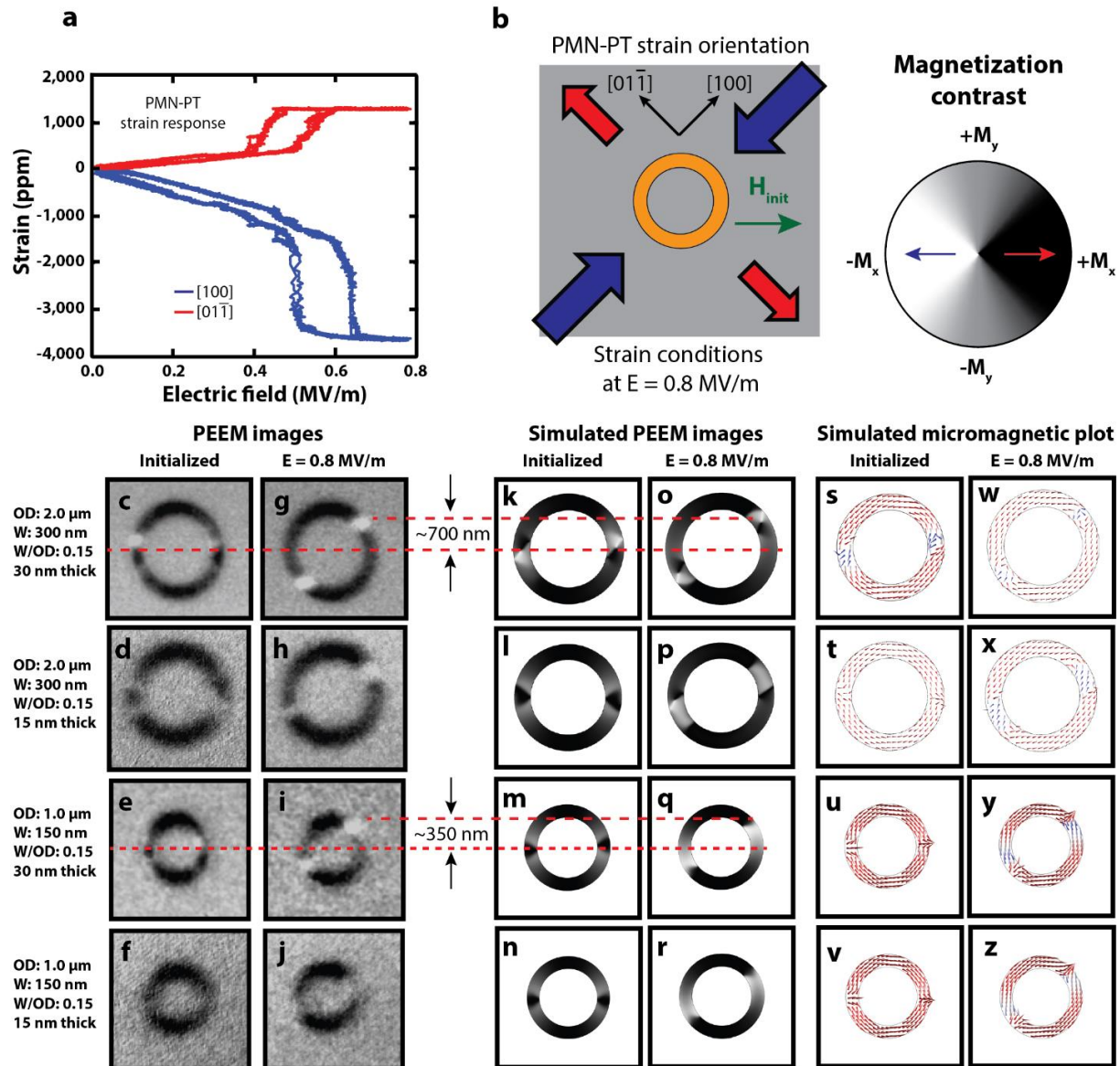
Figure 13 Electrically-driven sub-micron domain wall rotation (a) A strain response along the [100] and [01$\bar{1}$] directions of a PMN-PT substrate as a function of an out-of-plane electric field. (b) Schematic illustrating the initialization field (H_{init}) direction with respect to the PMN-PT [100] and [01$\bar{1}$] directions and the compressive and tensile strain response along each direction at 0.8 MV/m. c-j) XMCD-PEEM images showing the initialized (c-f) and electrically rotated (g-j) onion states in 30 and 15 nm thick rings with OD = 2 µm, W = 300 nm and OD = 1 µm, W = 150 nm. k-r) Simulated images from the coupled micromagnetic/elastodynamic model of initialized (k-n) and electrically rotated (o-r) rings with identical dimensions to the rings in parts c-j. The color scale contrast of the simulated micromagnetic orientation is scaled to match the contrast obtained with XMCD-PEEM. s-z) Micromagnetic plots from the same simulations shown in parts k-r showing the orientation of individual grid elements from the model. Red and blue arrows indicate the relative orientation direction. Dashed red lines are eye guides and indicate the domain wall displacement for each ring after strain is applied.

With the magnetic response to an applied electric field induced strain measured, we now investigate the magnetic response as a function of Ni thickness and electric field cycling. Ramping the electric field down to 0 MV m^{-1} produces different final magnetic states depending on the ring thickness, which can be explained in terms of induced strain. All the rings are subject to shear lag effects[48, 49], where strain varies through a structure as a function of position from a free edge. This shear lag effect is well known in the mechanics community studying finite size structures. These shear lag effects attenuate the influence of the magnetoelastic coupling as a function of ring thickness. It is also important to point out that XMCD-PEEM is a surface sensitive technique which measures the magnetic orientation of only the top few nanometers in the rings[50]. In Figure 14a-n, PEEM images are shown for a 2 µm OD, 300 nm wide ring of each thickness (15, 30, and 45 nm) at different applied electric fields. The domain walls in the 45 nm thick ring (Figure 14a, b) do not exhibit large movements in response to the electric field induced strain. Upon applying the electric field, the relatively thicker ring has a large shear lag dependence producing more inhomogeneous strains which reduce the effective strain present at the Ni surface. Thus, we do not observe significant domain wall motion. Both the presence of an inhomogeneous strain state and the inability to electrically move domain walls in 45 nm thick rings has been confirmed with the micromagnetic/elastodynamic model.
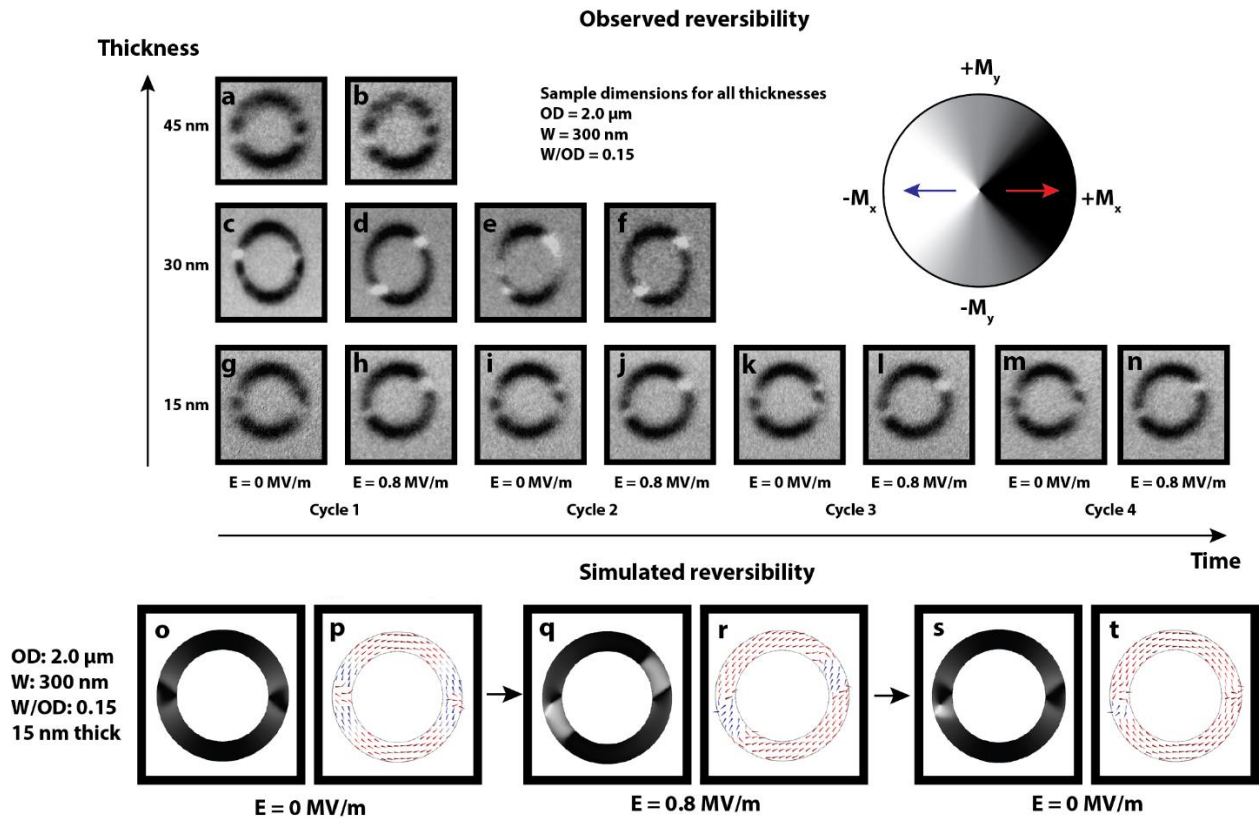
Figure 14 Thickness-dependent cycling behavior in Ni ring structures. Surface magnetic state for rings with identical lateral dimensions (2 μm OD, 300 nm width) but with varying thicknesses 45 nm (a and b); 30 nm (c-f); and 15 nm (g-n) plotted as a function of electric field cycling. (a and b) The 45 nm thick ring displays little to no rotation behavior upon the initial cycle. (c-f) For 30 nm thick rings, we observe a domain wall rotation after the first cycle; however, the rotated domain broadens back toward its initial state as the electric field is removed. This is due to magnetic relaxation, possibly driven by local remanent strains, in the rings as the strain is removed. Cycling the 30 nm thick ring a second time reproduces the rotated onion state state. (g-n) The 15 nm thick sample displays reproducible elastic domain wall rotation behavior over 4 cycles as a function of the applied electric field. (o-t) Simulated images (o, q, and s) and micromagnetic plots (p, r, and t). Parts o and p show an initialized 15 nm thick, 2 μm OD, and 300 nm width ring. Parts q and r demonstrate magnetic domain wall motion and broadening as a result of a simulated electric field of 0.8 MV/m. Parts s and t illustrate that the magnetization returns to a state similar to the initialized state shown in parts o and p after the simulated electric field is removed.

As the thickness of the ring is reduced from 45 nm to 30 nm, the domain wall movement response to the electrically-driven strain becomes more significant (Figure 14c-f). This domain wall movement in the 30 nm ring is directly related to both the larger effective surface strain (reduced shear lag) as well as the presence of a more homogeneous strain state through the thickness. As can be seen in Figure 14d, the domain wall was successfully rotated by 45° toward the PMN-PT [100] axis. Applying strain in this case introduces a tunable source of magnetoelastic energy that competes with the existing shape anisotropy and exchange energies of the initialized rings to reorient the magnet. As tensile strain, along the $[01\bar{1}]$ axis, and compressive strain, along the [100] axis, increase, an easy axis is created along the [100] axis due to the inverse magnetostriction effect. This increases the magnitude of the magnetoelastic energy, which is proportional to $\cos^2 \theta$ where θ is the angle between the magnetization and the compressive strain direction, making the Ni structures more energetically favorable to rotate toward the [100] axis. This occurs as long as the change in the total magnetic energy due to the magnetoelastic energy outweighs any significant changes to the exchange or demagnetization energies present during reorientation. As shown in Figure 13, and Figure 14c,d for 30 nm thick rings, and Figure 14g and h for 15 nm thick rings, when a strain is transferred more uniformly through the thickness of the ring the onion states are more likely to rotate toward the new magnetic energy minimum generated along the PMN-PT [100] axis.

In Figure 14e, we observe magnetic domains broadening when the electric field is removed instead of remaining stationary. This broadening suggests that an elastic force is present that drives a portion of the domain back towards its initial position. As previously stated, we have assumed the Ni rings are initially unstrained and removal of the electric field should not provide such a driving force. As shown in Figure 13a, we expect reducing the electric field

40

returns the sample to a zero strain state, thus removing the contribution of magnetoelastic energy to the overall magnetic energy. Assuming the exchange and shape anisotropies remain constant and the absence of remanent strain, reducing the magnetoelastic energy should not alter the magnetic domain wall orientation stabilized along the new energy minimum. Thus, this observation of domain broadening suggests a re-evaluation of the zero initial strain assumptions is required.

It is important to note that the influence of the electric field induced strain on the magnetization of the fabricated structures critically depends on the initial value of the strain imposed on the Ni structures at the time of deposition[17]. While the samples were pre-poled prior to the Ni deposition step[25], the Ni rings still remain subject to local strain variations due to the presence of micron scale ferroelectric domains in the PMN-PT[17]. It is reasonable to assume that the 1 and 2 μm OD Ni rings from our samples span multiple PMN-PT ferroelectric domains which may be oriented along the two out-of-plane <111> polarization directions and along the four in-plane <111> polarization directions. A reorientation of these domains along different vectors after deposition and fabrication of the Ni rings (*e.g.* due to the application of electric field) generates a localized remanent strain that has been previously reported[17, 25]. Although, we believe it is unlikely, another source of remanent strain may be attributed to our fabrication process. After pre-poling the PMN-PT substrates, Ni films were electron-beam evaporated onto these substrates at a process temperature of approximately 50 °C. This temperature might have partially de-poled the substrate (*i.e.* reoriented the surface <111> polarizations) resulting in a small remanent strain[26].

Re-evaluating our system leads to the following assertion. Initializing the rings into the onion state first creates a stable magnetization state in the presence of unintentional localized remanent strains. Applying an electric field initially drives an onion state toward a new orientation based along the dominant PMN-PT strain axis, as discussed before. However, when the electric field is removed, rather than return to a net zero strain state it returns to a localized remanent strain which provides a back driving force that serves to relax the local magnetization towards its initial position and metastable energy minimum. Thus, the final magnetic state observed in the 30 nm thick rings (Figure 14**Error! Reference source not found.**e) consists of a omain broadened between the strain-generated easy axis along the PMN-PT [100] direction and the initialized magnetic direction which is 45° from the [100] direction.

The 15 nm thick rings are subject to similar local strain cycling conditions; however, in this case the relatively thinner layer (compared to the 30 nm thick rings) reduces the magnetic relaxation degrees of freedom by favoring a more dominant exchange contribution to the total magnetic energy at the expense of both the demagnetization energy and the electrically-generated magnetoelastic energy contributions[42]. The strain-induced magnetoelastic energy does not dominate the total magnetic energy for these rings, instead it perturbs the magnetic domain to rotate slightly toward the [100] axis (Figure 14h) at 0.8 MV m^{-1}. Removing the electric field appears to return the magnetic domain back to its original position (Figure 14i). It is most likely driven back to its original state by the additional magnetic stiffness imposed by the exchange and demagnetization conditions for this thickness as well as any unintentional remanent strain contributions. Cycling the electric field in the 15 nm thick ring case (Figure 14g-n) confirms the repeatability of this apparent elastic domain wall behavior.

The elastic domain wall broadening that we observe in Figure 14e in the 30 nm thick ring and the cyclical domain wall reorientation that we observe in Figure 14g-n in the 15 nm thick ring are a result of the total magnetic energy rebalancing after the strain is tuned through multiple cycles. This magnetic energy minimization process, induced by tuning the magnetoelastic energy, forms the basis of the coupled micromagnetic/elastodynamic model used to verify the PEEM results in Figure 13. We note that these simulations assume no initial strain and do not account for the remanent strain and ferroelectric domains we experimentally observed. The majority of our simulations did not exhibit the elastic relaxation behavior we observe with PEEM. Instead, the magnetic domains remained fixed in their new positions. This is why we have attributed the observed relaxation behavior to remanent strain. However, one simulation of a 15 nm thick, 2 µm OD, 300 nm wide ring (Figure 14o-t) produced an elastic behavior despite the lack of initial and remanent strain built into the model. It serves as an example to demonstrate the magnetically stiff conditions in the 15 nm thick samples, created by the higher exchange energy contribution, which can contribute to the elastic behavior of the domain wall as a function of electric field cycling. After initializing the onion state (Figure 14o,p), the additional magnetoelastic energy produced by a simulated electric field of 0.8 MV m^{-1} creates an easy axis (and energy minimum) 45° relative to the magnetic initialization axis and along the [100] direction (Figure 14q,r). A domain forms in the simulation with domain walls at both the new energy minimum along the [100] direction and along the initialized direction. Removing the simulated electric field decreases the magnitude of the magnetoelastic energy in the system and the relative exchange and demagnetization energies drive the domain to elastically return to its original configuration (Figure 14s,t). We observe a relaxation of the magnetization back to an energy condition similar to (but not identical with) the initialized state.

3.4 Concluding Remarks

We conclude that the 45 nm thick rings, for the diameters studied, are too thick to adequately transfer the strain to alter the magnetic energy landscape (i.e. shear lag effect). The initialized domain walls in 30 nm thick rings, for the ring diameters studied, are sensitive to the electrically-driven strain, but their relatively large thickness creates a less constricted magnetic environment that leaves these rings susceptible to local environmentally-generated strains. Finally, magnetic domains in the 15 nm thick rings, for the ring diameters studied, also show electrically-driven domain wall behavior, but in this case the constricted magnetic environment leads to an elastic-like domain reorientation upon cycling. We also note that based on the initial orientation of the domain walls with respect to the PMN-PT [100] direction we can choose to deterministically rotate the domain walls clockwise or counter-clockwise. Though we only show data for one helicity, experiments for both helicities were performed and showed identical but symmetric behavior. Finally, we note that the sample geometries used in this work are capable of producing piecewise, sub-micron domain wall displacements, 700 and 350 nm in the 2 and 1 µm OD rings (Figure 13c, g and Figure 13e, i), without the assistance of an external magnetic field.

CHAPTER 4

CONTROL OF MAGNETIZATION USING PZT SUBSTRATES

4.1 PZT based multiferroic heterostructures

In the previous chapter, we showed 45˚ rotation of onion state in Ni ring structures using single crystal PMN-PT substrate. Additional rotation of the SD state beyond the initial 45˚ step requires the generation of strains in multiple angles. The possibility of this is suggested by recent studies[27-30], which analytically simulated the generation of orthogonal localized strains on a 500 nm thick PZT film with six surface patterned electrodes[28]. When applying a 10 MV/m electric field between the electrode pair and bottom of the PZT film, ~1000 ppm of in-plane anisotropic strain is generated at the center of the top surface of the electrodes, enabling manipulation of the magnetic state in a single ring structure[28].

In this study, we use 300 μm thick polycrystalline PZT substrates (PZT 610HD from TRS Technologies) and pattern eight surface electrodes on the substrate (Figure 15a). The polycrystalline PZT substrates show negligible macroscopic crystalline anisotropy, so they are suitable to generate in-plane isotropic strains with the surface electrodes. Depending on the thickness of a piezoelectric material, the optimal electrode distance to generate maximum strain varies. As opposed to the thin film PZTs in previous studies[28-30], which have ~ 1 μm electrode distance and non-uniform strain applied on the ferromagnetic structures, the bulk substrates allow a larger dimension of surface electrodes that generates a more uniform strain

near a substantially larger center area. The larger central strained area makes possible control and

observation of multiple SD states at the same time, by placing multiple disks in this center area.

Lastly, the eight surface patterned electrodes induce in-plane orthogonal strains every 45˚, which

apply the maximum magnetoelastic effective field to SD state at each strain application step.
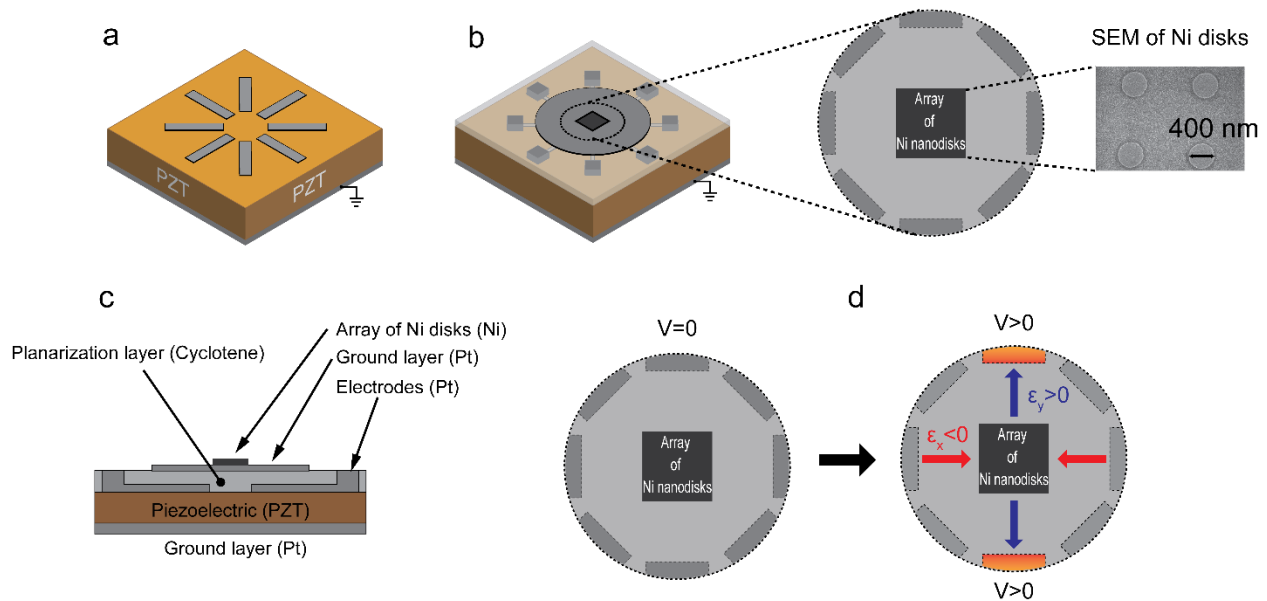
Figure 15 Schematic of sample and generation of anisotropic in-plane strain. a. Schematic of the PZT substrate with patterned electrodes. The top surface has 8 electrodes to generate anisotropic in-plane strains in steps of 45°. The backside of the PZT has a Pt ground layer.; b. Schematic of the multiferroic heterostructure that consists of the PZT substrate with patterned electrodes; planarization layer; ground layer; an array of Ni nanodisks. Inset 1: Detailed configuration of Ni disks in the center of the underlying electrodes. Inset 2: SEM image of 15 nm thick, 400 nm OD Ni disks; c. Cross-sectional view of the multiferroic heterostructure. ; d. Generation of anisotropic strain with an application of electric field on one electrode pair. Anisotropic in-plane strain is generated by applying a voltage on one underlying electrode pair

4.1.1 Challenges with PZT substrates

Fabricating surface electrodes and Ni nanodisks on PZT substrates and characterizing their magnetic states present two crucial challenges. First, the PZT substrate has average surface roughness of 2.83 nm with peak roughness greater than 20 nm (Figure 16 and Table 3), attributed to the presence of polycrystalline grains[51]. The rough surface could cause magnetic pinning in thin film magnetic structures, impeding reorientation of the SD state. Second, the exposed surface electrodes cause issues with measurement. The exposed surface electrodes emit stray electric fields when a voltage is applied to them, which might affect electric-field-sensitive micromagnetic measurements such as X-ray photoemission electron microscopy (X-PEEM), magnetic force microscopy (MFM), and scanning electron microscopy with polarization analysis (SEMPA). For MFM, the measurement method used here, stray electric fields impose electrostatic force on a MFM tip, altering the movement of the tip.

In order to overcome the problems of surface roughness and stray electric fields, we add a planarization layer to flatten the surface of the PZT substrate and a top grounding layer to shield the stray electric fields. After patterning electrodes on a PZT substrate, we spin-coat a 3 μm thick benzocyclobutene (BCB) layer as an insulator and planarization layer followed by a deposition of 5 nm Al/5 nm Ti/50 nm thick Pt layer (radius of 3 mm) as a top grounding plane (Figure 15b). The Pt layer provides a ground plane to shield stray electric field for stable measurement. On top of the Pt layer, an array of 15 nm thick, 400 nm diameter Ni disks is fabricated in the center of the underlying electrodes by electron beam lithography (Figure 15c). With the planarization and the ground layer, the average surface roughness of 0.586 nm nm with peak roughness of 5.30 nm (Figure 15, Figure 16 and Table 3). In addition, the BCB layer has the electrical breakdown field

of 500 MV/m. Therefore, the 3 μm thick BCB layer is able to withstand an electric field up to

1500 V.
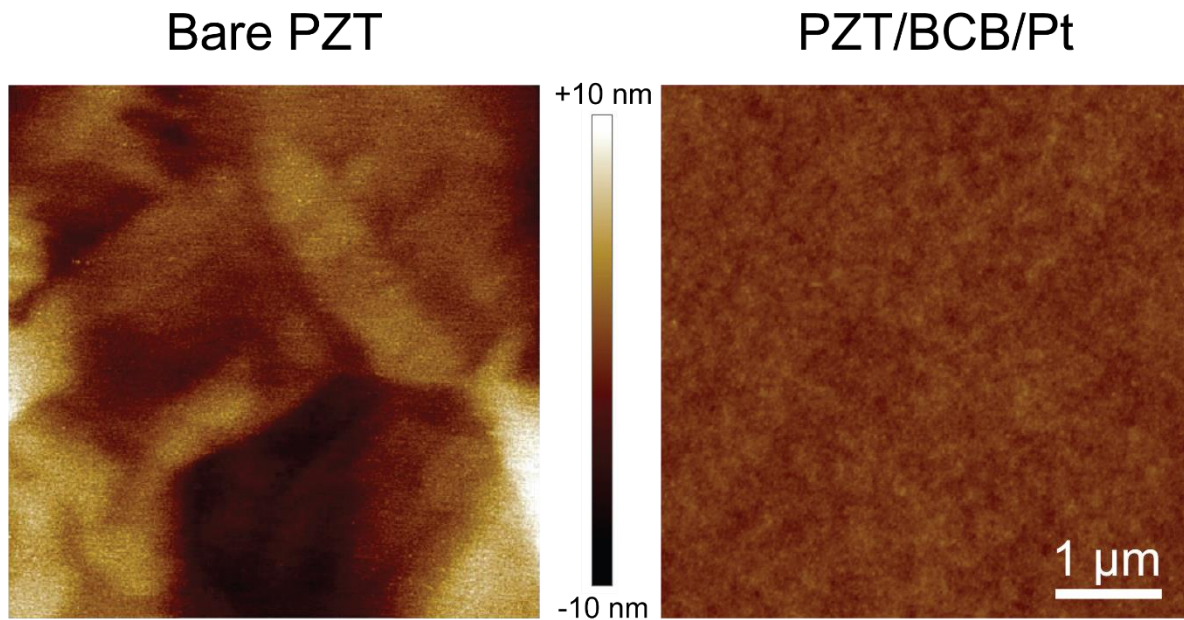
Figure 16 AFM results of a bare 300 μm thick PZT substrate and PZT/BCB/Pt structure.

Table 3 Comparison of PZT and PZT/BCB/Pt in surface roughness

	Bare PZT [nm]	PZT/BCB/Pt[nm]
Ra (Arithmetic average)	2.83	0.586
Rq (Root mean square)	2.19	0.467
Rmax (Maximum peak to peak)	20.3	5.30

4.2 Fabrication process

The multiferroic heterostructure is fabricated using 3 optical lithography processes and 1 electron beam lithography. On the back side of a PZT 610HD substrate (W 10 mm x H 10 mm x T 0.3 mm), a 10 nm Ti/ 50 nm Pt ground layer is deposited by electron beam evaporation (Figure 17a). With the first optical lithography/lift-off process, eight 10 nm Ti/40 nm Pt/10 nm Al surface electrodes are patterned on the front side by electron beam evaporation. A 3 μm thick BCB planarization layer is then spin-coated on top of the PZT substrate and vacuum-cured at 250˚C for 3 hours (Figure 17c). A second optical lithography process and 5:1 O2/CF4 plasma etching open the 8 electric contacts for wire bonding (Figure 17d). After patterning the center ground plane and the electric pads with a third optical lithography, a 5 nm Al/ 5 nm Ti/50 nm Pt layer is evaporated on the center area and the contacts (Figure 17e). The Al layers improve adhesion to the BCB, and the Ti layers promote adhesion to the PT, Ni and PZT substrate. Lastly, electron beam lithography defines 400 nm OD disk structures in the middle, and a 3 nm Ti/15 nm Ni disks are fabricated with electron beam evaporation and lift-off process (Figure 17f). In the electron beam lithography process, a double-resist technique (MMA EL-6/PMMA 950) is used for better sidewall profile of the Ni structures. The cross-sectional view of the final structure is shown in Figure 17g.

a

e

b

f

SEM of Ni disks

10 mm

400 nm

c

Planarization layer
(Cyclotene)

Array of Ni disks (Ni)
Ground layer (Pt)
Electrodes (Pt)

d

g

Piezoelectric (PZT)
Ground layer (Pt)
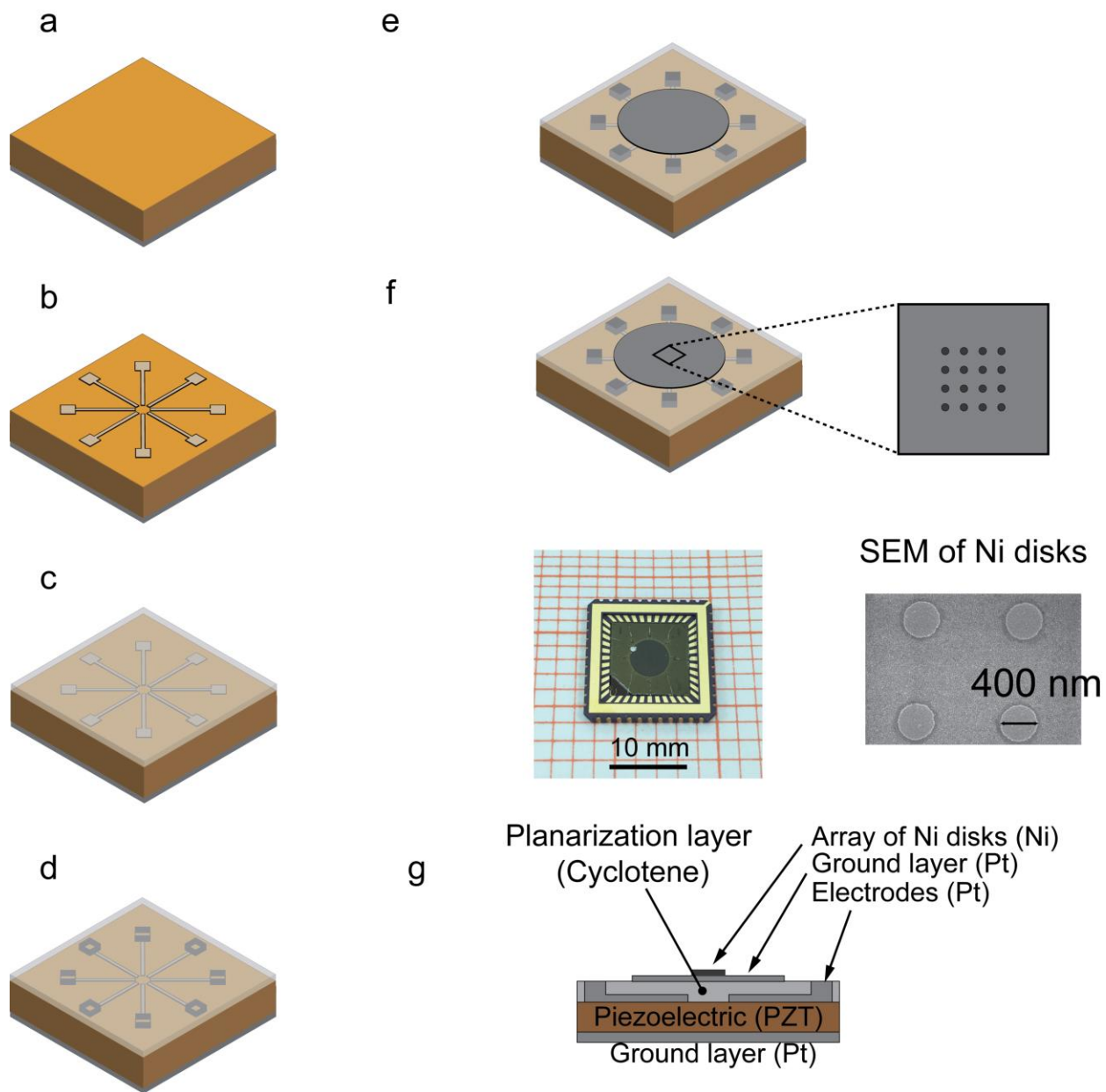
Figure 17 Fabrication process flow of PZT-based multiferroic heterostructure

4.3 Finite element analysis

We first characterize the strain response in the multiferroic heterostructure using a finite element model. Figure 18a shows the schematic of the multiferroic heterostructures without Ni disks. Eight Pt surface electrodes, 60 nm thick, are defined on a 300 μm thick PZT substrate. To maximize the generation of in-plane anisotropic strain for the 300 μm thick PZT substrates, we first find the optimal electrode configuration, specifically the width of the electrodes and the distance between opposing electrode pairs. First, as long as the electrodes do not overlap together, wider electrodes are desirable to increase area that has uniform strain configuration, in the space between the electrodes. The wider area with uniform strain also allows more Ni structures in the middle area. Second, the optimal electrode distance varies with the thickness of the PZT substrate. When the distance is too close (d < 40 μm in Figure 19), the middle area is more affected by out-of-plane deformation of the active electrodes. When the distance is too far (d > 120 μm in Figure 19), the piezoelectric deformation from the active electrode has little effect in the middle area. Therefore, the optimal distance should be calculated to generate maximum in-plane anisotropic strain in the middle area. The optimal distance between the electrode pairs is obtained by varying the width and distance in the finite element model. The width of the electrode, w, is linearly scaled with the electrode distance, d_{elec}, so as not to be overlapped together, given as

$$w = \text{Round}\left[\frac{d_{elec} - 16.544 \cdot 10^{-6}}{2.414 \cdot 10^{-6}}\right] [\mu m] \tag{8}$$

For example, 60 μm, and 100 μm of the electrode distances give 18 μm, and 35 μm wide electrodes, respectively.

51

The average strain in the middle sweet spot at 1.33 MV/m is measured and plotted in Figure S2. The optimal electrode distance for the 300 μm thick PZT is found between 60 μm and 100 μm. In this study, we choose the 18 μm wide electrodes/60 μm electrode distance.
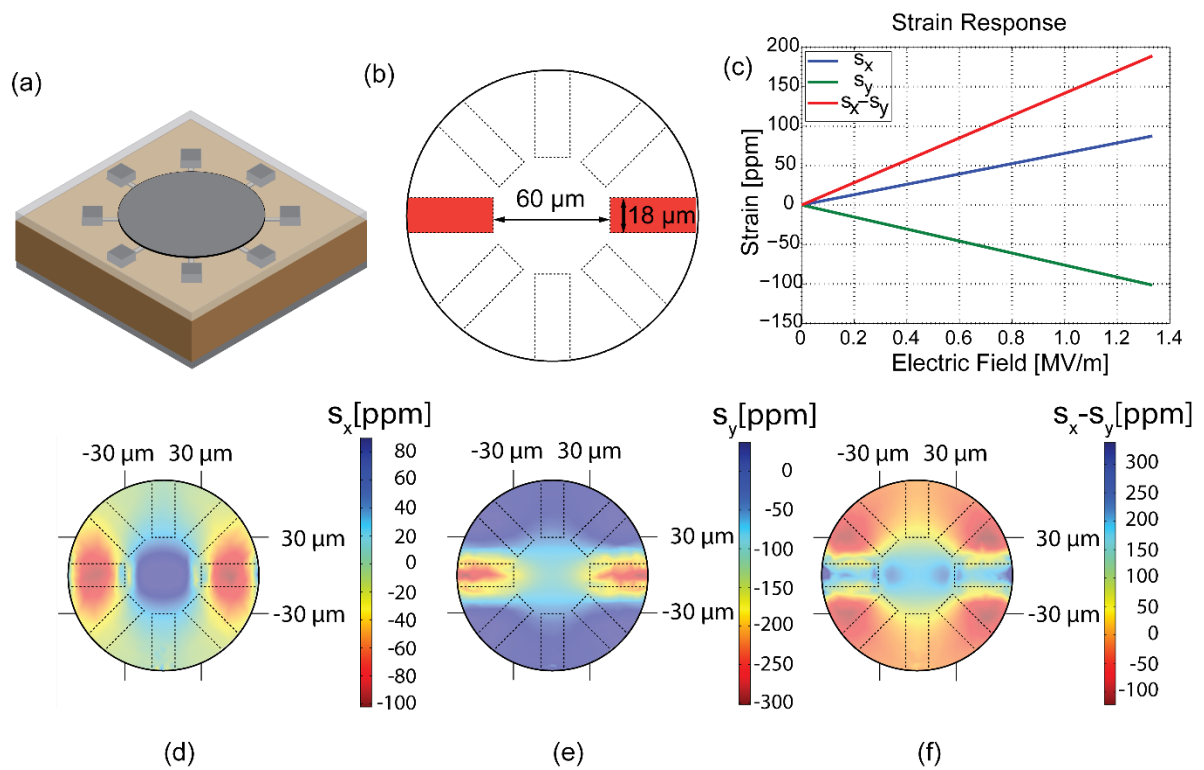
Figure 18 Finite element analysis: strain response of the multiferroic heterostructure with a voltage applied (a) Schematic of the multiferroic heterostructure. (b) Geometry of the underlying electrodes. The enabled electrodes are highlighted in red color.; (c) Average strain response of the center area, 15 μm x 15 μm, with an electric field.; (d) Strain profile in x at 1.33 MV/m; (e) Strain profile in y at 1.33 MV/m; (f) Differential strain profile at 1.33 MV/m
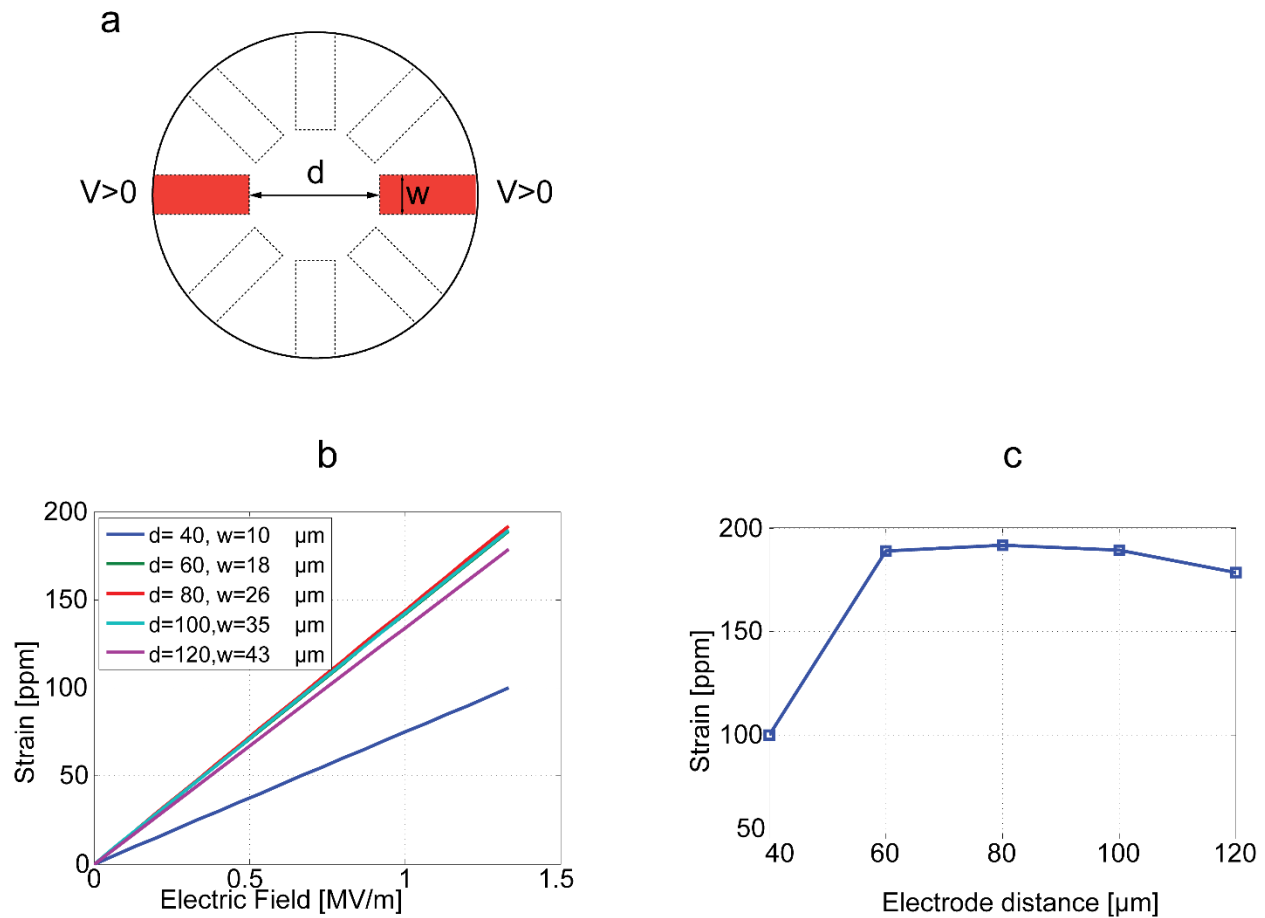
Figure 19 Optimization of the configuration of surface electrode (a) the schematic of the surface electrodes. The optimal electrode distance, *d*, and the electrode width, w, are found for a 300 μm thick PZT substrate (b) average differential strain, $(s_x - s_y)$, response of varying geometries with electric field. (c) detailed comparison of average differential strain, $(s_x - s_y)$, at 1.33 MV/m, taken from Figure 19b.

On top of the electrodes and the PZT substrate, layers of 3.0 μm thick BCB and 60 nm thick Pt are patterned. A voltage is applied to one electrode pair (highlighted in Figure 18b), and the rest of the electrodes and the bottom side of the PZT are grounded. In Figure 18c, the strain response on the top Pt surface is calculated by averaging strains in the center 15 μm x 15 μm area, where Ni disks are fabricated. At 1.33 MV/m (400 V across 300 μm thick PZT substrate), the center area of interest experiences a +90 ppm of tensile strain ($s_x > 0$) along the active

electrodes (standard deviation, σ_x= 1.70 ppm), and -100 ppm of compressive strain ($s_y <$ 0) normal to the active electrodes (standard deviation, σ_y= 3.91 ppm). The strain profiles in the x and y axis at 1.33 MV/m are shown Figure 18d and e. The average differential strain, $s_x - s_y$, at 1.3MV/m is +190 ppm, as presented in Figure 18f. By applying a voltage on the other electrode pair, the result shows generation of symmetric, in-plane orthogonal strains with respect to the active electrode pair. Therefore, four different in-plane orthogonal strains can be generated by separately enabling each electrode pairs: compressive strain along 0°/180°, 45°/225°, 90° /270°, and 135°/315° and tensile strain perpendicular to the compressive strain.

The magnetoelastic behavior in Ni disks with thickness of 15 nm and diameter of 400 nm is predicted by the following micromagnetic/elastodynamic simulation[33] that couples the electrically generated strains with SD states in the disks. The four different orthogonal strains with 1.33 MV/m that are obtained from the previous finite element model are sequentially applied to the Ni disk. In Figure 20a', prior to the strain application, an initial SD state is created in the Ni disk after saturating the Ni disk magnetization in the +x axis. Then, the first anisotropic strain that is created by applying a voltage to the A-A' pair (Figure 20b). The anisotropic strain induces a new easy axis in the direction of compressive strain, +45°, reorienting the magnetization toward the easy axis. After releasing the strain, the exchange interaction work in cooperation with the demagnetization field to form the stable SD state in 45° (Figure 20b'). In Figure 20c'-e', further rotations are shown with different stain application steps and removal.
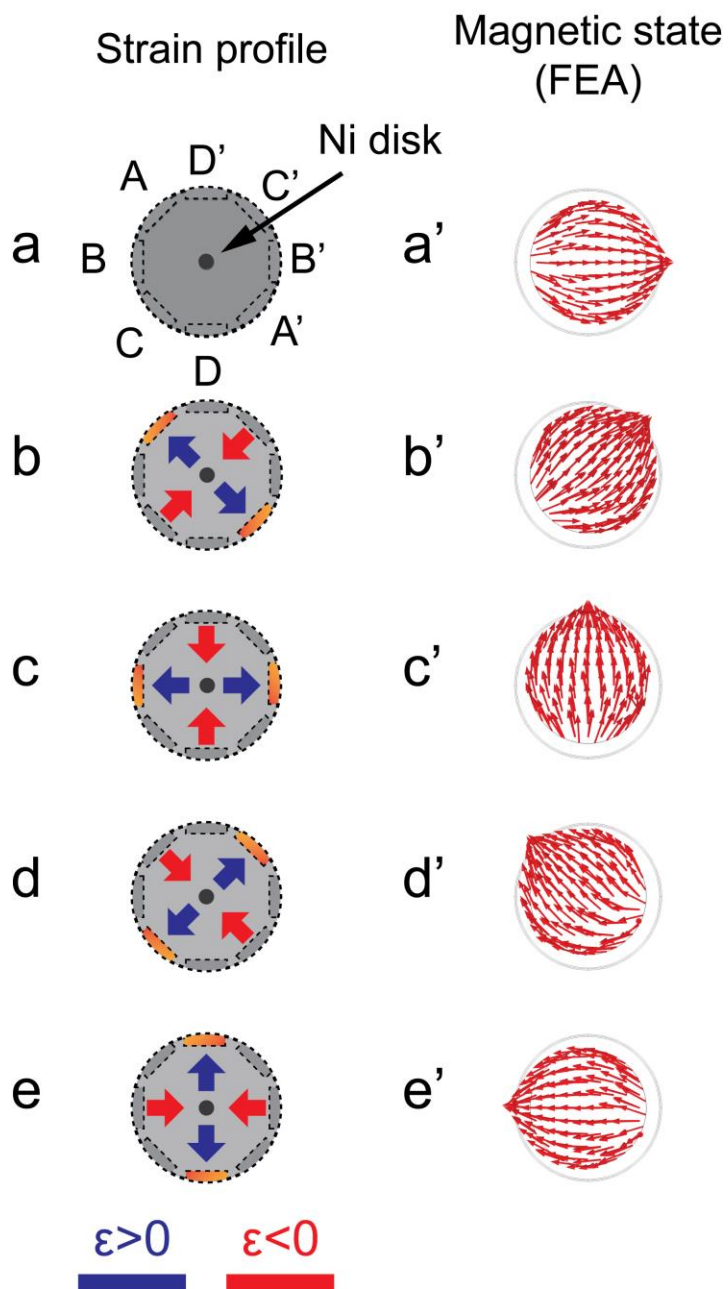
Figure 20 Finite element analysis of magnetoelastic response in a Ni disk with thickness of 15 nm and diameter of 400 nm. (a)-(e) strain configuration with sequential voltage application steps (a') Initial magnetic SD state in the Ni disk (b')-(e') FEA simulation results of magnetoelastic responses in the Ni disk.

4.4 Experimental results

4.4.1 PEEM results

We fabricated 15 nm thick, 2 μm OD nickel structures, disks and rings. The ring structures were initialized to form onion states by applying 3 kOe of an external magnetic field (Figure 21.2a). The first electrode pair was then actuated by 0.66 MV/m to generate anisotropic in-plane strains in PEEM. Due to the negative magnetostrictive property of nickel, the domain walls are reoriented toward the compressive directions in -45˚ and -135˚ as shown in Figure 21.2b and Figure 21.3b. In Figure 21.2b, the onion state showed the 45˚ rotation, which we had seen in the Ni/PMN-PT experiment. Second, while the first electrode pair was on, another electric field was applied to the second electric pair to give a smooth transition of strain steps. Further domain wall motion was observed in the disk structures toward the new compressive strain (Figure 21.3c). We could not observe further rotation in the ring structures with further strain application. This is attributed to the presence of pinning effect caused by the imperfect edge, which has more impact on the ring structures. Lastly, the electric field on the first electrode pair was released, and this generated compressive strain in ±90˚. The domain turned more into grey in the left disk in Figure 21.3d and the domain wall between the black and grey domain became vertical, which verified the presence of vertical compressive strain.
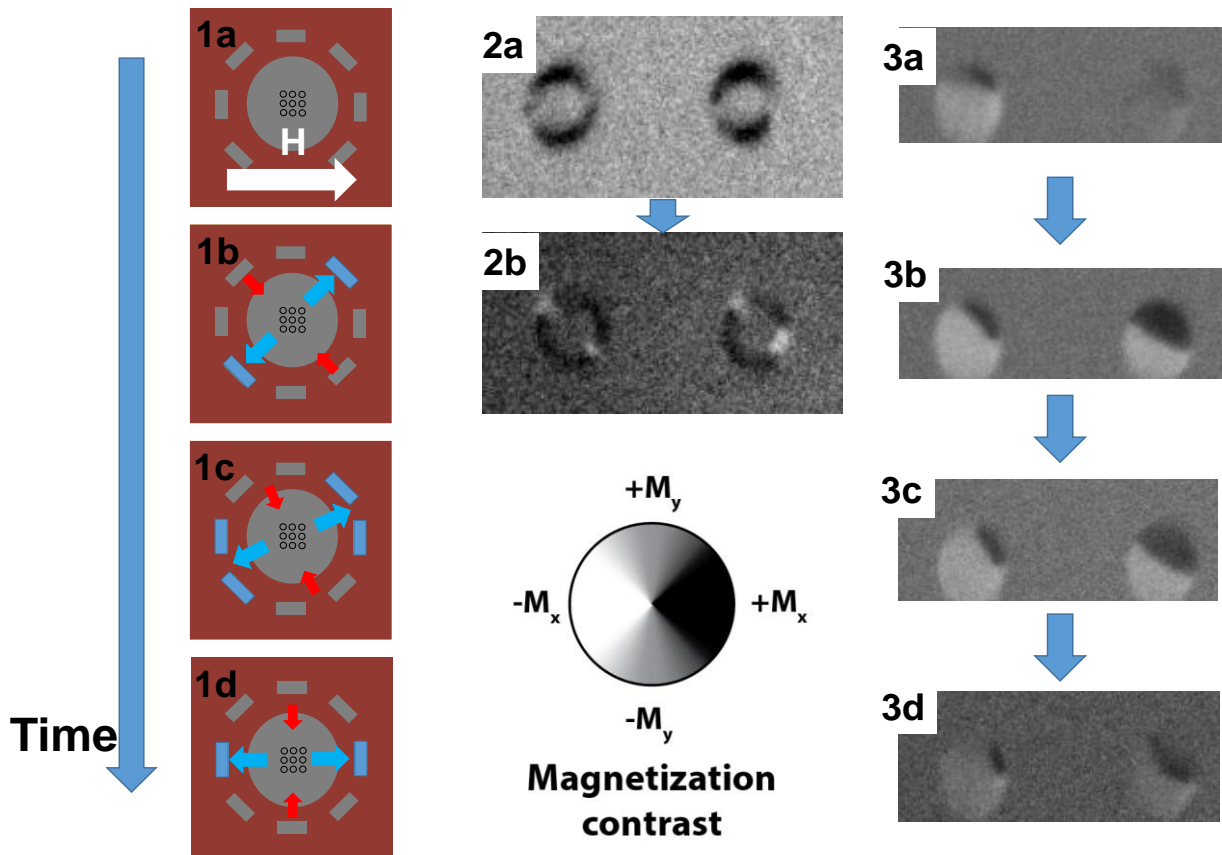
Figure 21 PEEM results of Ni rings and disks with applied strain (1) Measurement procedure of sample with patterned electrodes. (2a) Initial onion states in nickel rings (Outer diameter: 2.0 μm, Inner diameter: 1.4 μm). (2b) 45˚ rotation of onion states in Ni rings after applying orthogonal strains. (3) Domain wall motion in 2.0 μm disks with strain steps

4.4.2 MFM results

After the FEA simulations, we fabricate the multiferroic heterostructures and experimentally measure the step-wise 180˚ rotation of the SD State by MFM. Prior to the MFM measurement, a 3 kOe of external magnetic field is applied to 15 nm thick, 400 nm OD Ni disks to create a SD State. In Figure 22a', MFM shows the initial SD State in two Ni disks that are aligned at 0˚. Due to risks of electrical breakdown in the MFM system, each MFM image in Figure 22b'-e' is measured after applying 400 V from outside of the MFM. Figure 22b' shows

the rotation of SD State toward 45˚/225˚ after applying orthogonal strains generated by A-A' pair. In Figure 22c'-e', the SD States align with 90˚/270˚, 135˚/315˚, and 180˚/0˚ corresponding with a series of voltage applications on the remaining electrode pairs (B-B', C-C', and D-D', respectively). We are unable to observe further rotations in the two disks after the 180˚ rotation due to coupling of the magnetic MFM tip with the Ni disks, which alters the magnetic state in the Ni disks. We use low-momentum MFM tips (MESP-LM-V2 from Bruker) to minimize the magnetic interruption of the magnetic state, but magnetic interruptions are still observed during measurement. We also note that, in general, stepping rotations of SD states are observed in most of the disks. However, some of the SD states either fall in multi-domain state/vortex state, or are pinned after several steps of strain applications. We attribute these issues to the presence of defects, imperfect surface and edge as well as the undesired coupling with the MFM tip.
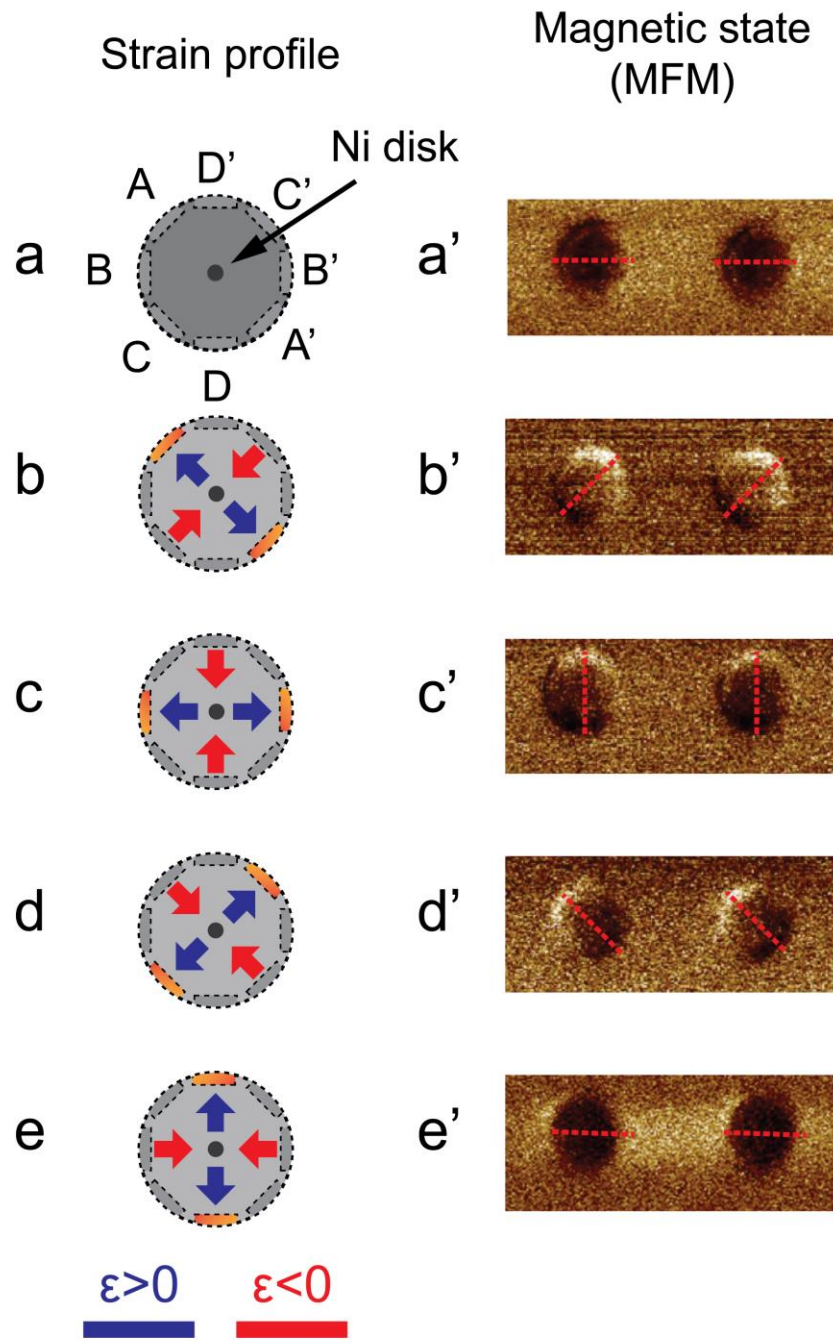
Figure 22 MFM results of magnetoelastic response in Ni disks with thickness of 15 nm and diameter of 400 nm. (a)-(e) strain configuration with sequential voltage application steps (a') Initial magnetic SD state in the Ni disk (b')-(e') MFM results of magnetoelastic responses in the Ni disks.

4.5 Concluding Remarks

In this chapter, multi-step rotation of magnetic states in Ni structures has been shown using multiferroic magnetoelastic coupling. The polycrystalline PZT substrate was chosen to generate isotropic strain in multiple directions. To alleviate the metrological issues resulted from the polycrystalline substrate, an intermediate polymer layer was introduced. The generation of multi-directional piezoelectric strains with surface patterned electrodes and the magnetoelastic behavior in the nanodisks were predicted by fully coupled multi-physics finite elements simulations. The PEEM and MFM experimental results showed the deterministic rotation of the magnetic states in agreement with the simulation results.

CHAPTER 5

FABRICATION OF TERFENOL-D MICROSTRUCTURES

5.1 Terfenol-D as a magnetostrictive material in multiferroic heterostructures

As we discussed in Chapter 1.2.1, Terfenol-D is known to have the highest magnetoelastic coefficient. The saturation magnetostriction of Terfenol-D is more than 25 times larger than that of Ni and the saturation magnetization of Terfenol-D is twice that of Ni. n the previous studies[52, 53], the Ni/PZT/Ni laminate[52] and the Terfenol-D/PZT/Terfenol-D laminate[53] showed the magnetoelectric coupling constant of 6-9 mVcm^{-1}Oe^{-1} and 4,800 mVcm^{-1}Oe^{-1}, respectively. Although Terfenol-D is a good alternative to maximize the magnetoelectric coupling in strain-mediated multiferroic structures, the usage of Terfenol-D is currently limited due to its highly reactive property, which makes difficult to fabricate nanoscale structures with the conventional fabrication techniques. Ty and Dy are electropositive metals that are highly reactive with water and the halogen elements.

5.2 Fabrication of Terfenol-D structures

We developed a new way to fabricate nanoscale Terfenol-D structures using 100% Ar ion etching and MaN-2403 e-beam resist. Firstly, a Ta/Terfenol-D/Ta film (barrier layer/ magnetostrictive material /capping layer) is deposited onto a piezoelectric substrate using a

magnetron sputtering (Figure 23a). MaN-2403 is a negative tone resist for e-beam lithography. It can resolve ~10 nm feature sizes, which is suitable to pattern fine shapes, such as rings with 50 nm width, and nanostructures. 300 nm thick MaN-2403 is spin-coated on the surface of the sample (Figure 23b). With e-beam lithography and development process, MaN etch mask that consists of nano- and microstructures are created (Figure 23c). Ar+ ion plasma is chosen to etch the reactive Terfenol-D film. Ar is a noble gas, which is most stable and non-reactive. Ar ion bombardment on Terfenol-D is 100% physical etching. Therefore, Ar ion plasma can anisotropically etch Terfenol-D (Figure 23d). After the etch process, the remaining etch mask is stripped with a Mr-Rem 700 resist stripper (Figure 23e). The fabricated 50 nm thick Terfenol-D structures are shown in Figure 24.
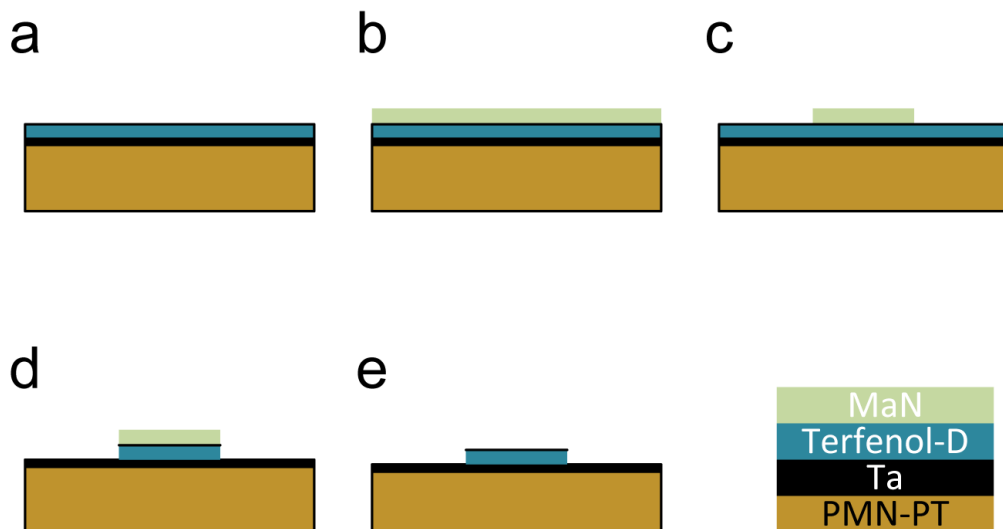
Figure 23 Terfenol-D fabrication process flow
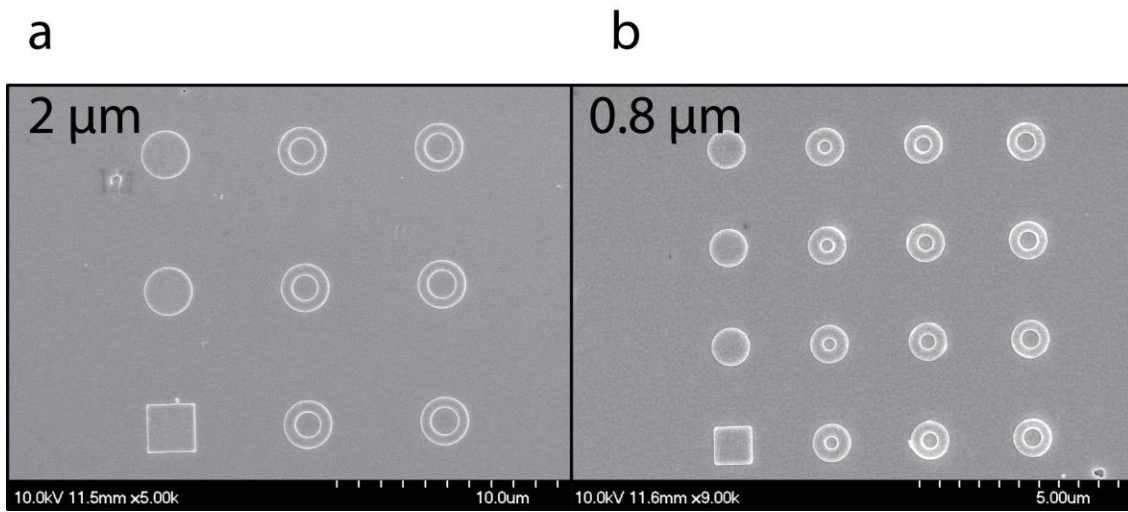
Figure 24 SEM of 50 nm thick Terfenol-D structures on a PMN-PT substrate. (a) 2 μm size Terfenol-D square, disks, and rings with varying widths. (b) 800 nm size Terfenol-D square, disks, and rings with varying widths

CHAPTER 6
CONCLUSION

In the present work, the control of magnetic domain in ferromagnetic Ni structures at the nano- and micro-scale was demonstrated. The multiferroic composites with ferromagnetic structures on a piezoelectric material were developed for such deterministic control. Electric field applied to the piezoelectric materials generated strain that coupled to the magnetic material and reshaped the magnetoelastic energy landscape in the magnetic structures. Magnetic states in ferromagnetic nano- and micro- structures were deterministically controlled with engineered piezoelectric strain

In Chapter 2, the characterization and control of the magnetic states in thin film Ni structures were investigated. To reliably obtain an onion state, the geometry of ring structures was both numerically and experimentally characterized with the finite element model and XMCD-PEEM. To maximize the magnetoelastic coupling with an applied strain, the optimal strain angle was calculated with the effective magnetoelastic field.

In Chapter 3, the deterministic domain wall rotation in ferromagnetic Ni rings on single-crystal PMN-PT substrates was presented. While imaging the Ni rings with XMCD-PEEM, an electric field was applied across the PMN-PT substrate, which induced strain in the ring structures that drove the rotation of the onion state toward the dominant PMN-PT strain axis by the inverse magnetostriction effect. The rotation of the onion states was analytically predicted using the fully coupled micromagnetic/elastodynamic finite element models, which verified the experimental behavior.

Chapter 4 demonstrated multi-step rotation of the magnetic magnetic domains in Ni structures using multiferroic magnetoelastic coupling. The isotropic multi-directional piezoelectric strain was generated with surface patterned electrodes on PZT piezoelectric ceramics. The generation of piezoelectric strain and the magnetoelastic behavior in the Ni structures are predicted by fully coupled multi-physics finite elements simulations. The experimental results show deterministic rotation of the magnetic domains in agreement with the simulation results.

Chapter 5 explored the fabrication of Terfenol-D structures to replace the Ni in the multiferroic heterotructures. To overcome its highly reactive property of Terfenol-D, the 100% physical Ar+ ion plasma etching process was developed, and the Terfenol-D nano- and microstructures were successfully fabricated. This new Terfenol-D structures are expected to maximize the magnetoelectri coupling and contribute to energy efficient multiferroic systems.

In summary, this new multiferroic approach to control of magnetism solely by electric field could open new ways to locally control magnetism at the nanoscale without the scaling limit imposed by Joule heating.

CHAPTER 7

REFERENCES

[1]   M. Bibes and A. Barthélémy, "Towards a magnetoelectric memory," *Nature materials,* pp. 425-426, 2008.

[2]   K. Wang, J.-M. Liu, and Z. Ren, "Multiferroicity: the coupling between magnetic and polarization orders," *Advances in Physics,* vol. 58, pp. 321-448, 2009.

[3]   I. De Vlaminck and C. Dekker, "Recent advances in magnetic tweezers," *Annual review of biophysics,* vol. 41, pp. 453-472, 2012.

[4]   J. Dobson, "Remote control of cellular behaviour with magnetic nanoparticles," *Nature nanotechnology,* vol. 3, pp. 139-143, 2008.

[5]   A. Tay, F. E. Schweizer, and D. Di Carlo, "Micro-and nano-technologies to probe the mechano-biology of the brain," *Lab on a Chip,* vol. 16, pp. 1962-1977, 2016.

[6]   C. Murray, E. Pao, P. Tseng, S. Aftab, R. Kulkarni, M. Rettig*, et al.*, "Quantitative Magnetic Separation of Particles and Cells Using Gradient Magnetic Ratcheting," *Small,* vol. 12, pp. 1891-1899, 2016.

[7]   P. Tartaj, M. del Puerto Morales, S. Veintemillas-Verdaguer, T. González-Carreño, and C. J. Serna, "The preparation of magnetic nanoparticles for applications in biomedicine," *Journal of Physics D: Applied Physics,* vol. 36, p. R182, 2003.

[8]   R. Hao, R. Xing, Z. Xu, Y. Hou, S. Gao, and S. Sun, "Synthesis, functionalization, and biomedical applications of multifunctional magnetic nanoparticles," *Advanced Materials,* vol. 22, pp. 2729-2742, 2010.

[9]   D. Niarchos, "Magnetic MEMS: key issues and some applications," *Sensors and Actuators A: physical,* vol. 109, pp. 166-173, 2003.

[10]   T. M. Liakopoulos and C. H. Ahn, "A micro-fluxgate magnetic sensor using micromachined planar solenoid coils," *Sensors and Actuators A: Physical,* vol. 77, pp. 66-72, 1999.

[11] E. Rapoport, D. Montana, and G. Beach, "Integrated capture, transport, and magneto-mechanical resonant sensing of superparamagnetic microbeads using magnetic domain walls," *Lab on a chip,* vol. 12, pp. 4433-4440, 2012.

[12] J. M. Hu, L. Q. Chen, and C. W. Nan, "Multiferroic heterostructures integrating ferroelectric and magnetic materials," *Advanced Materials,* vol. 28, pp. 15-39, 2016.

[13] W. Eerenstein, N. D. Mathur, and J. F. Scott, "Multiferroic and magnetoelectric materials," *Nature,* vol. 442, pp. 759-65, Aug 17 2006.

[14] N. A. Spaldin and M. Fiebig, "The renaissance of magnetoelectric multiferroics," *Science,* vol. 309, pp. 391-392, 2005.

[15] R. Ramesh and N. A. Spaldin, "Multiferroics: progress and prospects in thin films," *Nature materials,* vol. 6, pp. 21-29, 2007.

[16] J. Ma, J. Hu, Z. Li, and C. W. Nan, "Recent progress in multiferroic magnetoelectric composites: from bulk to thin films," *Advanced Materials,* vol. 23, pp. 1062-1087, 2011.

[17] M. Buzzi, R. Chopdekar, J. Hockel, A. Bur, T. Wu, N. Pilet*, et al.*, "Single domain spin manipulation by electric fields in strain coupled artificial multiferroic nanostructures," *Physical review letters,* vol. 111, p. 027204, 2013.

[18] J. L. Hockel, A. Bur, T. Wu, K. P. Wetzlar, and G. P. Carman, "Electric field induced magnetization rotation in patterned Ni ring/Pb (Mg1/3Nb2/3) O3](1− 0.32)-[PbTiO3] 0.32 heterostructures," *Applied Physics Letters,* vol. 100, p. 022401, 2012.

[19] H. Ahmad, J. Atulasimha, and S. Bandyopadhyay, "Reversible strain-induced magnetization switching in FeGa nanomagnets: Pathway to a rewritable, non-volatile, non-toggle, extremely low energy straintronic memory," *Scientific reports,* vol. 5, 2015.

[20] C.-W. Nan, M. I. Bichurin, S. Dong, D. Viehland, and G. Srinivasan, "Multiferroic magnetoelectric composites: Historical perspective, status, and future directions," *Journal of Applied Physics,* vol. 103, p. 031101, 2008.

[21] V. Sampath, N. D'Souza, D. Bhattacharya, G. M. Atkinson, S. Bandyopadhyay, and J. Atulasimha, "Acoustic-wave-induced magnetization switching of magnetostrictive

nanomagnets from single-domain to nonvolatile vortex states," *Nano Letters,* vol. 16, pp. 5681-5687, 2016.

[22] N. D'Souza, M. S. Fashami, S. Bandyopadhyay, and J. Atulasimha, "Experimental Clocking of Nanomagnets with Strain for Ultralow Power Boolean Logic," *Nano Letters,* vol. 16, pp. 1069-1075, Feb 2016.

[23] H. Sohn, M. E. Nowakowski, C.-y. Liang, J. L. Hockel, K. Wetzlar, S. Keller*, et al.*, "Electrically driven magnetic domain wall rotation in multiferroic heterostructures to manipulate suspended on-chip magnetic particles," *ACS nano,* vol. 9, pp. 4814-4826, 2015.

[24] J. L. Hockel, S. D. Pollard, K. P. Wetzlar, T. Wu, Y. Zhu, and G. P. Carman, "Electrically controlled reversible and hysteretic magnetic domain evolution in nickel film/Pb(Mg1/3Nb2/3)O3]0.68-[PbTiO3]0.32 (011) heterostructure," *Applied Physics Letters,* vol. 102, p. 242901, 2013.

[25] T. Wu, P. Zhao, M. Bao, A. Bur, J. L. Hockel, K. Wong*, et al.*, "Domain engineered switchable strain states in ferroelectric (011) [Pb(Mg1/3Nb2/3)O3](1−x)-[PbTiO3]x (PMN-PT, x≈0.32) single crystals," *Journal of Applied Physics,* vol. 109, p. 124101, 2011.

[26] S.-E. Park and T. R. Shrout, "Ultrahigh strain and piezoelectric behavior in relaxor based ferroelectric single crystals," *Journal of Applied Physics,* vol. 82, pp. 1804-1811, 1997.

[27] J. Cui, J. L. Hockel, P. K. Nordeen, D. M. Pisani, C.-y. Liang, G. P. Carman*, et al.*, "A method to control magnetism in individual strain-mediated magnetoelectric islands," *Applied Physics Letters,* vol. 103, p. 232905, 2013.

[28] C.-Y. Liang, A. E. Sepulveda, D. Hoff, S. M. Keller, and G. P. Carman, "Strain-mediated deterministic control of 360° domain wall motion in magnetoelastic nanorings," *Journal of Applied Physics,* vol. 118, p. 174101, 2015.

[29] J.-M. Hu, T. Yang, K. Momeni, X. Cheng, L. Chen, S. Lei*, et al.*, "Fast magnetic domain-wall motion in a ring-shaped nanowire driven by a voltage," *Nano letters,* vol. 16, pp. 2341-2348, 2016.

[30] J. Cui, C.-Y. Liang, E. A. Paisley, A. Sepulveda, J. F. Ihlefeld, G. P. Carman, *et al.*, "Generation of localized strain in a thin film piezoelectric to control individual magnetoelectric heterostructures," *Applied Physics Letters,* vol. 107, p. 092903, 2015.

[31] R. Kellogg, A. B. Flatau, A. Clark, M. Wun-Fogle, and T. A. Lograsso, "Temperature and stress dependencies of the magnetic and magnetostrictive properties of Fe 0.81 Ga 0.19," *Journal of applied physics,* vol. 91, pp. 7821-7823, 2002.

[32] M. Donahue and D. Porter, "Oommf user's guide, version 1.0, interagency report nistir 6376," *National Institute of Standards and Technology, Gaithersburg, MD,* 1999.

[33] C.-Y. Liang, S. M. Keller, A. E. Sepulveda, A. Bur, W.-Y. Sun, K. Wetzlar, *et al.*, "Modeling of magnetoelastic nanostructures with a fully coupled mechanical-micromagnetic model," *Nanotechnology,* vol. 25, p. 435701, 2014.

[34] A. Doran, M. Church, T. Miller, G. Morrison, A. T. Young, and A. Scholl, "Cryogenic PEEM at the Advanced Light Source," *Journal of Electron Spectroscopy and Related Phenomena,* vol. 185, pp. 340-346, 2012.

[35] C. Chen, F. Sette, Y. Ma, and S. Modesti, "Soft-x-ray magnetic circular dichroism at the L 2, 3 edges of nickel," *Physical Review B,* vol. 42, p. 7262, 1990.

[36] J. Feng, A. MacDowell, R. Duarte, A. Doran, E. Forest, N. Kelez, *et al.*, "An aberration corrected photoemission electron micorscope at the advanced light source," *Lawrence Berkeley National Laboratory,* 2003.

[37] S. Li, D. Peyrade, M. Natali, A. Lebib, Y. Chen, U. Ebels, *et al.*, "Flux closure structures in cobalt rings," *Physical Review Letters,* vol. 86, p. 1102, 2001.

[38] C. A. F. Vaz, T. J. Hayward, J. Llandro, F. Schackert, D. Morecroft, J. A. C. Bland, *et al.*, "Ferromagnetic nanorings," *Journal of Physics: Condensed Matter,* vol. 19, p. 255207, 2007.

[39] M. Hara, T. Kimura, and Y. Otani, "Controlled depinning of domain walls in a ferromagnetic ring circuit," *Applied physics letters,* vol. 90, p. 242504, 2007.

[40] M. Kläui, C. Vaz, L. Lopez-Diaz, and J. Bland, "Vortex formation in narrow ferromagnetic rings," *Journal of Physics: Condensed Matter,* vol. 15, p. R985, 2003.

[41]   M. Laufenberg, D. Backes, W. Bührer, D. Bedau, M. Kläui, U. Rüdiger, *et al.*, "Observation of thermally activated domain wall transformations," *Applied physics letters,* vol. 88, p. 052507, 2006.

[42]   R. D. McMichael and M. J. Donahue, "Head to head domain wall structures in thin magnetic strips," *Magnetics, IEEE Transactions on,* vol. 33, pp. 4167-4169, 1997.

[43]   E. Rapoport and G. Beach, "Transport dynamics of superparamagnetic microbeads trapped by mobile magnetic domain walls," *Physical Review B,* vol. 87, p. 174426, 2013.

[44]   T. Wren, B. Gribkov, V. Petrashov, and O. Kazakova, "Phase diagram of magnetic states in nickel submicron disks," *Journal of Applied Physics,* vol. 118, p. 023906, 2015.

[45]   G. Herzer, "Nanocrystalline soft magnetic materials," *Journal of Magnetism and Magnetic Materials,* vol. 112, pp. 258-262, 1992.

[46]   M. Weiler, A. Brandlmaier, S. Geprägs, M. Althammer, M. Opel, C. Bihler, *et al.*, "Voltage controlled inversion of magnetic anisotropy in a ferromagnetic thin film at room temperature," *New Journal of Physics,* vol. 11, p. 013021, 2009.

[47]   S. W. Choi, R. T. Shrout, S. J. Jang, and A. S. Bhalla, "Morphotropic phase boundary in Pb (MgNb) O3-PbTiO3 system," *Materials Letters,* vol. 8, pp. 253-255, 1989.

[48]   C.-M. Chang and G. P. Carman, "Experimental evidence of end effects in magneto-electric laminate composites," *Journal of Applied Physics,* vol. 102, p. 124901, 2007.

[49]   C.-M. Chang and G. P. Carman, "Modeling shear lag and demagnetization effects in magneto-electric laminate composites," *Physical review B,* vol. 76, p. 134116, 2007.

[50]   J. Stöhr and H. C. Siegmann, "Magnetism," *Solid-State Sciences. Springer, Berlin, Heidelberg,* p. 441, 2006.

[51]   C. Wang, "Investigation of Sputtered Ferroelectric Thin Films on Silicon Substrates," Ph.D. Dissertation, Carnegie Mellon University PA, 2007.

[52]   S. N. Babu, T. Bhimasankaram, and S. Suryanarayana, "Magnetoelectric effect in metal-PZT laminates," *Bulletin of Materials Science,* vol. 28, pp. 419-422, 2005.

[53]   J. Ryu, A. V. Carazo, K. Uchino, and H.-E. Kim, "Magnetoelectric properties in piezoelectric and magnetostrictive laminate composites," *Japanese Journal of Applied Physics,* vol. 40, p. 4948, 2001.